

High Temperature B2 Precipitation in Ru-Containing Refractory Multi-principal Element Alloys



CAROLINA FREY, HAOJUN YOU, SEBASTIAN KUBE, GLENN H. BALBUS, KAITLYN MULLIN, SCOTT OPPENHEIMER, COLLIN S. HOLGATE, and TRESA M. POLLOCK

Ru-based B2 phases present an opportunity to design two-phase BCC + B2 refractory multi-principal element alloys (RMPEAs) with higher temperature stability compared to B2 phases observed in RMPEAs. In this investigation, seven equiatomic Ru-containing RMPEAs were characterized in the as-cast and annealed conditions. Of the two Hf-free alloys, $\text{Mo}_{25}\text{Nb}_{25}\text{Ta}_{25}\text{Ru}_{25}$ was determined to be a single-phase B2 alloy and $\text{Mo}_{20}\text{Nb}_{20}\text{Ta}_{20}\text{W}_{20}\text{Ru}_{20}$ was single-phase BCC. Within all five Hf-containing alloys, phases formed during solidification included HfRu–B2, disordered BCC, and HfO_2 phases. The Hf-containing alloys also precipitated B2 nanoparticles within the BCC phases after further cooling in the solid. All phases were still present after annealing at 1500 °C to 1600 °C. The HfRu–B2 nanoparticles in as-cast $\text{Hf}_{20}\text{Mo}_{20}\text{Nb}_{20}\text{Ta}_{20}\text{Ru}_{20}$ were characterized by transmission electron microscopy (TEM), and a lattice misfit of < 1 pct between the BCC phase and B2 nanoparticles was calculated. Room-temperature micropillar compression tests were performed on BCC + B2 nanoparticle regions in annealed $\text{Hf}_{20}\text{Mo}_{20}\text{Nb}_{20}\text{Ta}_{20}\text{Ru}_{20}$. Post-mortem TEM analysis revealed precipitate shearing by dislocations, resulting in paired dislocations, along with bowing of dislocations around precipitates. Utilizing the insights from this investigation, compositions for RMPEAs with solutionable B2 precipitates stable above 1200 °C are suggested.

<https://doi.org/10.1007/s11661-024-07368-x>

© The Minerals, Metals & Materials Society and ASM International 2024

I. INTRODUCTION

REFRACTORY multi-principal element alloys (RMPEAs) are a new class of materials with the potential to replace current Ni- and Co-based superalloys in high temperature environments. Derived primarily from the nine refractory metals (Cr, Hf, Mo, Nb, Ta, Ti, V, W, and Zr), RMPEAs have much higher melting points than Ni and Co, increasing the potential operating temperatures of a resulting alloy if a similar balance of properties can be engineered. While refractory alloys were extensively investigated during the mid-to-late 1900s,^[1–3] the expansion from a

single-principal element to multiple-principal elements in the last decade offers greater opportunities to tailor alloy properties.

Stemming from the original “high entropy” hypothesis, RMPEAs have historically been designed as single-phase materials.^[4] However, single-phase RMPEAs reported in the literature to date have not yet demonstrated the balance of properties necessary for critical engineering components that operate at high temperature. For instance, alloys derived from the Hf–Nb–Ta–Ti–V–Zr system can be lightweight, exhibit extensive tensile ductility, and are capable of being highly cold worked, but their yield strengths rapidly decline near 1200 °C due to their relatively low melting points.^[5–8] Large additions of Mo and W significantly increase high temperature strength but are severely detrimental to the fabricability and tensile ductility of the resulting alloys.^[2,9,10] Cr and Al are frequently introduced for improving oxidation resistance and light weighting but form brittle intermetallic phases during aging or during high temperature testing.^[11–13] While information regarding the creep behavior of RMPEAs is limited, pure BCC metals generally exhibit inferior creep properties relative to FCC-based alloys, presenting another challenge to designing alloys with equivalent strength across a wide range of temperatures.^[14] Despite its much

CAROLINA FREY, HAOJUN YOU, SEBASTIAN KUBE, KAITLYN MULLIN, COLLIN S. HOLGATE, and TRESA M. POLLOCK are with the Materials Department, University of California, Santa Barbara, CA 93106. Contact e-mail: cfrey@ucsb.edu GLENN H. BALBUS is with the Air Force Research Laboratory, Materials and Manufacturing Directorate, Wright-Patterson AFB, OH 45433. SCOTT OPPENHEIMER is with the General Electric Global Research Center, Niskayuna, NY 12309.

Manuscript submitted September 4, 2023; accepted January 27, 2024.

Article published online April 4, 2024

higher solidus temperature (T_s), $\text{Hf}_{20}\text{Nb}_{20}\text{Ta}_{20}\text{Ti}_{20}\text{Zr}_{20}$ ($T_s = 1937\text{ }^\circ\text{C}$) exhibits much lower tensile creep strength compared to the matrix phase of the Ni-based superalloy CMSX-4 ($T_s = 1400\text{ }^\circ\text{C}$) at $980\text{ }^\circ\text{C}$.^[15] These limitations have inspired interest in the introduction of coherent secondary phases that are thermodynamically and morphologically stable at desired operating temperatures, which currently range between $1300\text{ }^\circ\text{C}$ and $1500\text{ }^\circ\text{C}$.^[16]

Potential strengthening phases for a disordered BCC RMPEA include B2 or $L2_1$ -Heusler intermetallics that are derived from the BCC lattice. RMPEAs with significant additions of Al, Ti, and Zr have demonstrated microstructures of highly coherent BCC phases within a B2 matrix that closely mimic the cuboidal γ/γ' microstructures in Ni- and Co-based superalloys.^[17–20] These lightweight alloys can exhibit higher specific compressive strengths compared to Ni-based superalloys such as IN718 and MAR-M247 up to $1000\text{ }^\circ\text{C}$.^[17] Noting the inherent brittleness of an intermetallic matrix, inverting the microstructure to form B2 precipitates in a BCC matrix has shown promise for potentially achieving high tensile ductilities in (Al, Ti, Zr) BCC + B2 alloys.^[20–27] Further, coherent (Al, Ti, Zr) precipitates have been shown to be highly stable at $1000\text{ }^\circ\text{C}$ in $\text{Al}_{10}\text{Cr}_8\text{Mo}_{27.3}\text{Ta}_{27.3}\text{Ti}_{27.3}$, remaining below 100 nm in size after 1000 h .^[28] However, critically, (Al, Ti, Zr) B2 precipitates in a disordered BCC matrix have not been shown to be thermodynamically stable above $1200\text{ }^\circ\text{C}$ and the addition of significant amounts of Al and Zr can result in the formation of significant volume fractions of deleterious phases that form at intermediate to high temperatures.^[11,12,26,29–31]

Other B2 formers, such as Fe and Co, have been investigated. Knowles *et al.* introduced Fe for precipitation of TiFe B2 in equilibrium with a disordered W-rich BCC phase at $1250\text{ }^\circ\text{C}$.^[32] Similarly, Yurchenko *et al.* investigated the use of Co to form HfCo ^[33] and TiCo ^[34] B2 matrices in equilibrium with a (Mo,Nb)-rich disordered BCC phase. These B2 phases were shown to be stable to at least $1000\text{ }^\circ\text{C}$ (HfCo) and $1200\text{ }^\circ\text{C}$ (TiCo). None of these phases were shown to be coherent with the disordered BCC phase. Other microstructural investigations of high temperature B2 and $L2_1$ phases have been conducted by Ghosh *et al.* and Misra *et al.*, focusing on Al and platinum-group additions in ternary and quaternary Nb systems.^[35,36]

An alternative strategy to introduce B2 phases with high temperature stability is to use additions of Ru, a platinum-group metal that forms isomorphous B2 phases with six of the nine refractory metals (Hf, Nb, Ta, Ti, V, and Zr).^[37–42] Ru also forms a B2 phase with Al^[41] and Si,^[43] which are desirable alloying additions due to their low densities and beneficial impact on oxidation resistance. These binary B2 phases are thermodynamically stable to much higher temperatures than the (Al, Ti, Zr)-based B2 phases; for example, the BCC + B2 phase fields in the HfRu, TiRu, and ZrRu binaries extend up to $1610\text{ }^\circ\text{C}$, $1575\text{ }^\circ\text{C}$, and $1236\text{ }^\circ\text{C}$, respectively.^[39,42] A high volume fraction of a HfRu–B2 phase was recently shown to be stable up to $1575\text{ }^\circ\text{C}$ in $\text{Hf}_{20}\text{Nb}_{20}\text{Ta}_{20}\text{Ru}_{20}\text{Zr}_{20}$, suggesting the thermal stability

of the B2 phases in the binary systems is maintained in more complex solutions.^[44] However, the HfRu–B2 phase in $\text{Hf}_{20}\text{Nb}_{20}\text{Ta}_{20}\text{Ru}_{20}\text{Zr}_{20}$ was suggested to be stable up to the solidus temperature, an obstacle to uniformly distributing the B2 precipitates in a matrix *via* the solution and aging-processing pathway typically utilized for Ni-based superalloys. Further investigation of phase equilibria in these higher-order compositional spaces is necessary to determine if a high volume fraction of coherent fine-scale Ru-based B2 precipitates can be produced in a ductile matrix.

To further investigate the potential of Ru as a B2 former for RMPEAs, a series of equiatomic Ru-containing RMPEAs were characterized in the as-cast and annealed conditions: $\text{Mo}_{25}\text{Nb}_{25}\text{Ta}_{25}\text{Ru}_{25}$, $\text{Mo}_{20}\text{Nb}_{20}\text{Ta}_{20}\text{W}_{20}\text{Ru}_{20}$, $\text{Hf}_{33}\text{Mo}_{34}\text{Ru}_{33}$, $\text{Hf}_{25}\text{Mo}_{25}\text{Nb}_{25}\text{Ru}_{25}$, $\text{Hf}_{25}\text{Mo}_{25}\text{Ta}_{25}\text{Ru}_{25}$, $\text{Hf}_{20}\text{Mo}_{20}\text{Nb}_{20}\text{Ta}_{20}\text{Ru}_{20}$, and $\text{Hf}_{25}\text{Nb}_{25}\text{Ru}_{25}\text{W}_{25}$. Candidate materials for this analysis were drawn from a list of alloys produced by GE Research^[45] and were selected for their high Ru content. This investigation found HfRu–B2 phases to be stable to at least $1500\text{ }^\circ\text{C}$ in all alloys containing Hf. Nano-scale B2 precipitates were also observed in the disordered BCC phases of the Hf-containing alloys. TEM investigations of the as-cast $\text{Hf}_{20}\text{Mo}_{20}\text{Nb}_{20}\text{Ta}_{20}\text{Ru}_{20}$ alloy found the B2 nanoparticles are coherent with the surrounding BCC matrix. Micropillar compression experiments were conducted to investigate dislocation interactions with the HfRu–B2 phases. Implications for the design of BCC + B2 alloys are discussed.

II. METHODS

The selected alloys were arc melted in an inert atmosphere from elemental raw materials.^[45] For studying the thermal stability of the as-cast microstructures, the five Hf-containing alloys were encapsulated in individual Ta ampoules under vacuum and annealed in a vacuum furnace. The $\text{Hf}_{33}\text{Mo}_{34}\text{Ru}_{33}$ alloy was annealed at $1500\text{ }^\circ\text{C}$ for 40 hours. The remaining alloys, with the exception of $\text{Mo}_{20}\text{Nb}_{20}\text{Ta}_{20}\text{W}_{20}\text{Ru}_{20}$ and $\text{Mo}_{25}\text{Nb}_{25}\text{Ta}_{25}\text{Ru}_{25}$, were annealed at $1600\text{ }^\circ\text{C}$ for 40 h. NbTi foil was inserted into the ampoules to act as a getter. The samples were heated with a ramp rate of $0.25\text{ }^\circ\text{C/s}$ and cooled at the maximum rate of the furnace (initial cooling rate was $\approx 6.2\text{ }^\circ\text{C/s}$ and decreased with decreasing temperature).

Wavelength-dispersive X-ray fluorescence (WDXRF) measurements of the bulk alloy compositions were conducted with a Rigaku ZSX Primus IV and are presented in Table I. Interstitial contents were also measured by inert gas fusion (O and N) and combustion analysis (C), both performed by Northern Analytical, Inc. Due to sample quantity limitations, interstitial contents were not measured for $\text{Mo}_{25}\text{Nb}_{25}\text{Ta}_{25}\text{Ru}_{25}$, $\text{Hf}_{25}\text{Nb}_{25}\text{Ru}_{25}\text{W}_{25}$, and $\text{Hf}_{20}\text{Mo}_{20}\text{Nb}_{20}\text{Ta}_{20}\text{Ru}_{20}$. Microscopy samples were ground by SiC sandpaper to 800 grit and then polished with sequentially smaller diamond suspensions to $1\text{ }\mu\text{m}$ before finishing with vibratory polishing. Scanning electron microscopy (SEM) images were acquired on a ThermoFisher Apreo C microscope with backscatter electron (BSE) and

Table I. Chemical Composition (at. pct) and Interstitial Content (ppmw) of the Bulk As-Cast Alloys

Alloy	Hf	Mo	Nb	Ru	Ta	W	O	N
Mo ₂₅ Nb ₂₅ Ta ₂₅ Ru ₂₅	—	24.0	25.9	25.0	25.2	—	—	—
Mo ₂₀ Nb ₂₀ Ta ₂₀ Ru ₂₀ W ₂₀	—	18.5	21.7	21.5	20.1	18.2	276	30
Hf ₃₃ Mo ₃₄ Ru ₃₃	32.6	35.3	—	32.1	—	—	1040	30
Hf ₂₅ Mo ₂₅ Nb ₂₅ Ru ₂₅	25.5	24.7	25.6	24.3	—	—	858	77
Hf ₂₅ Mo ₂₅ Ta ₂₅ Ru ₂₅	27.8	23.9	—	23.7	24.7	—	744	57
Hf ₂₀ Mo ₂₀ Nb ₂₀ Ta ₂₀ Ru ₂₀	20.5	19.7	20.6	18.6	20.6	—	—	—
Hf ₂₅ Nb ₂₅ Ru ₂₅ W ₂₅	24.8	—	24.0	28.3	—	22.9	—	—

secondary electron (SE) contrast; energy-dispersive X-ray spectroscopy (EDS) with an EDAX Si-drift EDX detector was used to acquire chemical composition information. Electron probe microanalysis (EPMA, Cameca SX-100) equipped with wavelength-dispersive spectroscopy was used in some cases for higher-accuracy composition measurements. A focused beam, of 20 kV and 10 nA, was used to maximize the spatial resolution. Pure elemental standards were used, and the mounts were carbon coated to negate electron beam charging. All elements had a 30 seconds on-peak and 30 seconds off-peak collection time, with analyzing crystals of: LLIF for Hf and Ta, LPET for Ru and Mo, and PET for Nb. X-ray diffraction (XRD) patterns were obtained with a Panalytical Empyrean Powder Diffractometer using Cu K α radiation ($\lambda = 0.154$ nm). Bulk samples were mechanically polished to a surface finish of 12.5 μm or better prior to XRD. Lattice parameters were determined by Bragg's Law from the peak positions. Reported volume fractions were determined *via* point counting method according to ASTM standard E562 19e1.^[46] Each grid had more than 100 pts.

Thin foils of as-cast Hf₂₀Mo₂₀Nb₂₀Ta₂₀Ru₂₀ were prepared for transmission electron microscopy (TEM) by using the FIB lift-out method with a Ga⁺ ion beam in a FEI Helios Dualbeam Nanolab 600 equipped with an OmniProbe. TEM microstructural investigations were conducted in a FEI Talos F200X S/TEM operated at 200 kV. Selected area electron diffraction (SAED) patterns were captured to identify the phases present in the foil. Scanning transmission electron microscopy (STEM) with a high-angle annular dark-field (HAADF) detector was performed to elucidate nanostructural features in the foil. EDS was employed to determine the local chemical compositions using a SuperX detector and Velox software.

Micropillars were fabricated in Hf₂₀Mo₂₀Nb₂₀Ta₂₀Ru₂₀ after heat treatment at 1600 °C using a FEI Nova dualbeam FIB/SEM. Initially, annular wells with an inner diameter of 7.5 μm and an outer diameter of 35 to 50 μm were milled to ≈ 10 μm depths at an accelerating voltage of 30 kV and current of 21 nA. Circular fiducial markers were then milled into the top of each pillar and shaped to their final dimensions using the lathe method described by Uchic *et al.*^[47] at 30 kV and 93 pA. The final diameters of the micropillars ranged from 5.18 to 5.28 μm , with length-to-diameter aspect ratios of ≈ 2 . The crystal orientation for each micropillar was determined by

electron backscatter diffraction (EBSD) in a Thermo Fisher Scientific Apreo C SEM at an accelerating voltage of 20 kV using an Oxford Symmetry S2 detector. Post-deformation characterization of the slip traces was performed in a TFS Apreo C at 5 kV using a beam deceleration of 220 V, as described by Balbus *et al.*^[48]

Micropillar compression experiments were conducted in a MTS XP Nanoindenter with a 10 μm diamond flat punch. A 10^{-3} s⁻¹ initial strain rate was used for each sample, and experiments were performed to a total displacement of 500 nm (≈ 5 pct strain). Thin foils for (S)TEM characterization were prepared from a deformed micropillar, as described by Norfleet *et al.*^[49] and Balbus *et al.*,^[48] where the foil is extracted such that its normal is perpendicular to the slip plane of interest. The samples were thinned to ~ 80 nm in a FEI Nova dualbeam FIB/SEM with a final milling step at 5 kV. Finally, the sample was polished in a Fischione 1040 NanoMill at 600 eV, 100 pA to help reduce FIB damage. Conventional TEM and annular dark-field (ADF) STEM experiments were performed in a TFS Talos X (S)TEM at 200 kV. Burgers vectors were determined in a conventional TEM using g.b analysis. Dislocation trace analysis to determine dislocation line direction using ADF STEM images was performed using the pycotem package.^[50]

III. RESULTS

Microstructural observations of the as-cast alloys (utilizing both SEM and TEM) are described first, followed by an investigation of high temperature heat treatments on the Hf-containing alloys. In all alloys, the two major constituent phases are named in order of their solidification sequence (1 or 2) and are identified as either disordered BCC or as an ordered HfRu-B2 intermetallic. Following this, dislocation-precipitate reactions studied *via* micropillar compression experiments and TEM are reported. Overall, the investigated microstructures provide a promising pathway for the development of solution and ageable BCC + Ru-B2 alloys.

A. Microstructures of As-Cast Hf-Free Alloys

Mo₂₅Nb₂₅Ta₂₅Ru₂₅ and Mo₂₀Nb₂₀Ta₂₀W₂₀Ru₂₀ both exhibit dendritic solidification, resulting in segregation throughout the microstructure (Figure 1).

Compositional variations from the dendritic regions to the inter-dendritic regions were measured *via* SEM-EDS and are reported in Table III. In $\text{Mo}_{25}\text{Nb}_{25}\text{Ta}_{25}\text{Ru}_{25}$, Mo and Ta segregated to the dendrite core and Nb and Ru segregated to the inter-dendritic regions. $\text{Mo}_{20}\text{Nb}_{20}\text{Ta}_{20}\text{W}_{20}\text{Ru}_{20}$ exhibited segregation of Nb and Ru to the inter-dendritic regions and Mo and W to the dendrite core. Segregation of Ta was less pronounced, with a slightly elevated concentration in the inter-dendritic regions. The center of the dendrite core regions in $\text{Mo}_{20}\text{Nb}_{20}\text{Ta}_{20}\text{W}_{20}\text{Ru}_{20}$ was also enriched in Nb and depleted in Ta. The inter-dendritic regions of both alloys contain (Nb,Ta,O)-rich phases, indicating the formation of oxides, and a small amount of porosity. The pores and oxides are both black in backscatter electron contrast.

The XRD scan of $\text{Mo}_{20}\text{Nb}_{20}\text{Ta}_{20}\text{W}_{20}\text{Ru}_{20}$ exhibits a set of disordered BCC peaks (Figure 2), while the XRD scan for $\text{Mo}_{25}\text{Nb}_{25}\text{Ta}_{25}\text{Ru}_{25}$ exhibits additional B2 ordering peaks. Only one set of peaks is visible for each alloy, consistent with the lack of significant secondary phase formation observed *via* SEM. TEM diffraction also provides evidence for the B2 phase in $\text{Mo}_{25}\text{Nb}_{25}\text{Ta}_{25}\text{Ru}_{25}$ in both the dendrite core and inter-dendritic regions (Supplemental Figure 1). $\text{Mo}_{25}\text{Nb}_{25}\text{Ta}_{25}\text{Ru}_{25}$ can, therefore, be identified as a single-phase B2 alloy. While $\text{Mo}_{20}\text{Nb}_{20}\text{Ta}_{20}\text{W}_{20}\text{Ru}_{20}$ does not demonstrate the extra B2 peaks in XRD, the dendritic segregation in the microstructure resulted in regions where the Ru concentration is equivalent to that of $\text{Mo}_{25}\text{Nb}_{25}\text{Ta}_{25}\text{Ru}_{25}$, suggesting regions of $\text{Mo}_{20}\text{Nb}_{20}\text{Ta}_{20}\text{W}_{20}\text{Ru}_{20}$ could also be ordered. The lattice parameters of the identified phases are presented in Table II.

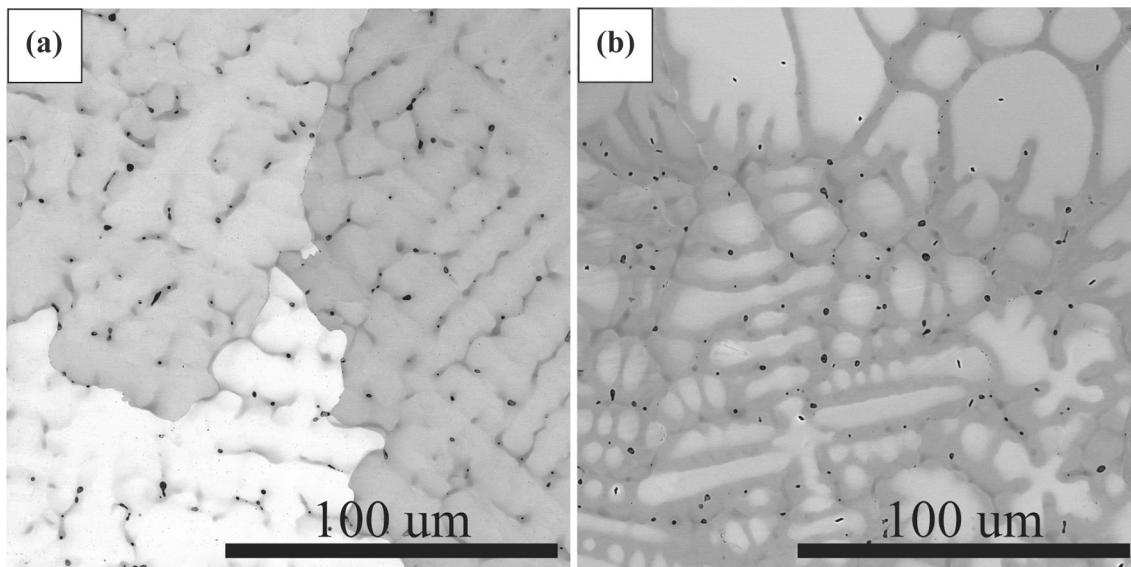


Fig. 1—BSE images of the microstructures of as-cast (a) $\text{Mo}_{25}\text{Nb}_{25}\text{Ta}_{25}\text{Ru}_{25}$ and (b) $\text{Mo}_{20}\text{Nb}_{20}\text{Ta}_{20}\text{W}_{20}\text{Ru}_{20}$. In both alloys, the spherical regions with black contrast are primarily (Nb,Ta,O)-rich phases. A minor number of the black regions are pores.

B. Microstructures of As-Cast Hf-Containing Alloys

1. $\text{Hf}_{33}\text{Mo}_{34}\text{Ru}_{33}$

Four phases are visible in the BSE microstructure images of $\text{Hf}_{33}\text{Mo}_{34}\text{Ru}_{33}$ (Figure 3): a light gray (Hf, Ru)-rich Phase 1, a dark gray (Mo)-rich Phase 2, a medium gray (Mo, Ru)-rich Phase 3, and a bright gray

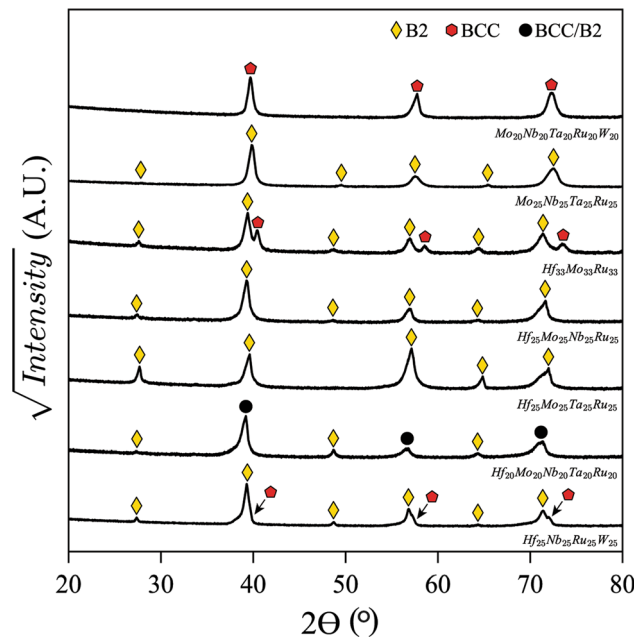


Fig. 2—XRD scans of the as-cast alloys. Only BCC and B2 peaks were observed. Asymmetry in the observed peaks may be the result of a low misfit between the BCC and B2 phases, causing overlapping peaks, or chemistry and lattice parameter variations within the disordered BCC phases. An example deconvolution of the peaks in as-cast $\text{Hf}_{20}\text{Mo}_{20}\text{Nb}_{20}\text{Ta}_{20}\text{W}_{20}\text{Ru}_{20}$ is provided in the Supplemental Materials and the remaining scans were not quantified further.

Table II. Identified phases and Calculated Lattice Parameters of the As-Cast Alloys

Alloy	Phase	Prototype	Lattice Parameter (Å)
Mo ₂₅ Nb ₂₅ Ta ₂₅ Ru ₂₅	B2	CsCl	3.194
Mo ₂₀ Nb ₂₀ Ta ₂₀ Ru ₂₀ W ₂₀	BCC	W	3.199
Hf ₃₃ Mo ₃₄ Ru ₃₃	B2	CsCl	3.232
	BCC	W	3.152
Hf ₂₅ Mo ₂₅ Nb ₂₅ Ru ₂₅	B2	CsCl	3.238
	BCC/B2	—	3.233
Hf ₂₅ Mo ₂₅ Ta ₂₅ Ru ₂₅	B2	CsCl	3.216
Hf ₂₀ Mo ₂₀ Nb ₂₀ Ta ₂₀ Ru ₂₀	B2	CsCl	3.246
	BCC/B2	—	3.242
Hf ₂₅ Nb ₂₅ Ru ₂₅ W ₂₅	B2	CsCl	3.240
	BCC	W	3.216

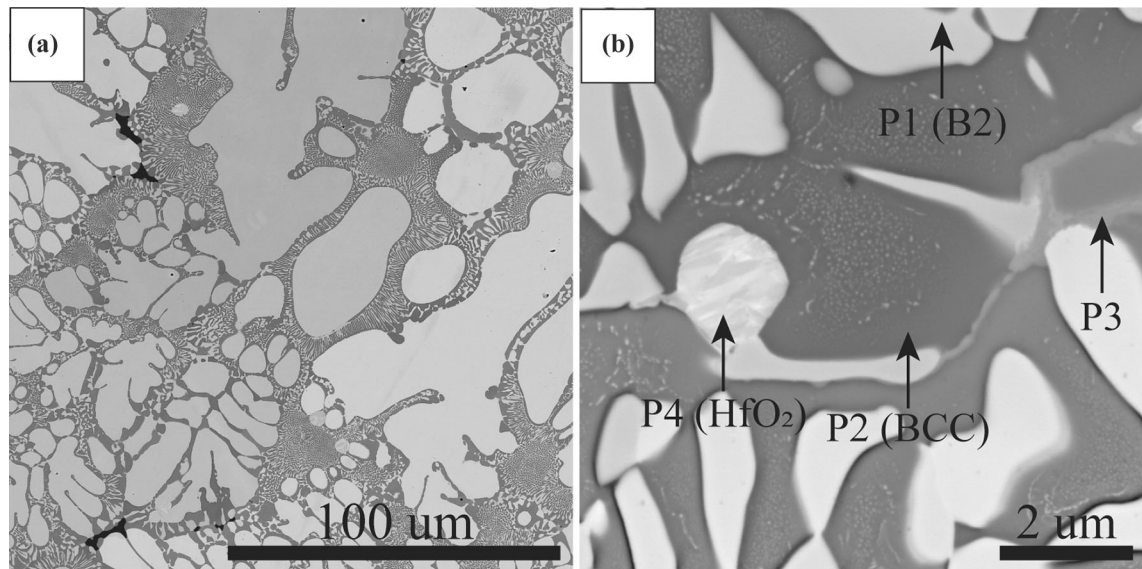


Fig. 3—(a) and (b) BSE images of the microstructure of as-cast Hf₃₃Mo₃₄Ru₃₃. Four phases are identified and present throughout the sample. Phase 1 nanoparticles are visible in the Phase 2 regions in (b). P1 is an ordered HfRu–B2 phase and P2 is a disordered (Mo)-BCC phase.

(Hf, O)-rich Phase 4 with internal striations. Phase 1 is present in three length scales in the microstructure, with similar *Z*-contrast in BSE and preferential polishing behavior in SE images at all length scales. Phase 1 is present as dendrites, in alternating lamellar regions with the dark gray Phase 2, and as nano-scale precipitates embedded in Phase 2. The two-phase lamellar region would be consistent with a eutectic reaction. Some nanoparticles appear coarsened and form chain-like structures but remain submicron in size. The combined area fraction (a_f) of the dendritic and lamellar Phase 1 is 0.62. Phase 2 is continuous throughout the microstructure and surrounds all three forms of Phase 1.

Phase 3 and Phase 4 are present in minor amounts (less than 0.10 area fraction). In some instances, Phase 4 is embedded in the Phase 1 dendrites, varying from submicron to 20 microns in diameter.

A XRD scan of the Hf₃₃Mo₃₄Ru₃₃ alloy is presented in Figure 2. Two sets of peaks are clearly visible: one set of peaks corresponds to a disordered BCC phase with no additional ordering peaks and the other set

corresponds to an ordered B2 phase. There are no ordered B2 phases found in the Mo–Ru^[51] or Hf–Mo^[52] binary-phase diagrams, and the composition of Phase 1 as measured by SEM-EDS corresponds to the composition of the ordered B2 intermetallic in the HfRu phase diagram.^[39] Therefore, Phase 1 is identified as a HfRu–B2 phase. While the composition of Phase 2 cannot be directly measured because of the nanoparticles, the uptake of Hf and Ru into the HfRu–B2 nanoparticles would result in a highly enriched Mo phase, and the calculated lattice parameter of Phase 2 (Table II) is close to the lattice parameter of pure Mo (3.152 Å vs 3.147 Å). Phase 2 is, therefore, identified as a disordered (Mo)-BCC phase. Due to their small volume fraction, no additional peaks are present to identify Phases 3 and 4. However, given the high O content of Phase 4 and the lack of significant amounts any elements other than Hf, it is identified as a hafnium oxide (HfO₂) phase.

Corresponding compositions of the phases are presented in Table III, with the exception of the dark

contrast (Mo)-rich BCC phase that was present in regions too small to probe with EDS. Compositions for the lamellar BCC and B2 inter-dendritic regions and the nanoparticle B2 + BCC regions are also presented. The composition of the B2 phase was also measured with EPMA and are presented in Table IV.

2. $Hf_{25}Mo_{25}Nb_{25}Ru_{25}$

Similar to $Hf_{33}Mo_{34}Ru_{33}$, $Hf_{25}Mo_{25}Nb_{25}Ru_{25}$ consists primarily of two phases (Figure 4): a (Hf, Ru)-rich Phase 1 that appears light gray in backscatter electron contrast and a second (Mo, Nb)-rich Phase 2 that is dark. Phase 1 solidified both as large blocky regions tens of microns across that are surrounded by a nano-scale layer of Phase 2 and as nano-scale fibrous rods alternating with Phase 2. This microstructure would be consistent with the formation of pro-eutectic Phase 1 surrounded by a fine-scale eutectic structure of Phases 1 and 2. When adjacent to the larger Phase 1 structures, the nano-scale Phase 1 is oriented with its longest direction perpendicular to the Phase 2 boundary. Layers of Phase 2 are also found independent of the large Phase 1 structures, resulting in the appearance of rings.

In some regions of the ingot, there is elongated phase morphology and coarsening of Phase 1 towards grain boundaries (Figures 4(b) and (d)). Larger regions of Phase 2 are also found at some grain boundaries. Within these regions there are patches of nano-scale precipitates embedded in Phase 2. Compositional segregation is evident, with the nano-scale particles appearing in regions enriched in Hf and Nb and depleted in Mo (Figures 5(a) and (b)). Some of the nanoparticles appear coarsened along a chain. Consistent with $Hf_{33}Mo_{34}Ru_{33}$, the nanoparticles demonstrate backscatter electron contrast and preferential polishing behavior in SE consistent with Phase 1, indicating that the nanoparticles and Phase 1 are the same phase. HfO_2 particles of similar composition and high O content to those observed in $Hf_{33}Mo_{34}Ru_{33}$ are also present with varying sizes and locations. The intergranular regions also contain a Hf-enriched phase (Phase 3) and a Nb-rich phase (Phase 4) with lower oxygen content than the HfO_2 particles. Phase 3 appears bright in backscatter contrast and is primarily composed of Hf, with an appreciable content of Nb (19.5 at. pct) and minor amounts of Mo and Ru. Phase 4 appears darker in backscatter electron contrast and is enriched in Nb, containing on average 49.6 at. pct Nb and 38.0 at. pct Hf and equivalent amounts of Mo and Ru as Phase 3.

A XRD scan of $Hf_{25}Mo_{25}Nb_{25}Ru_{25}$ is presented in Figure 2. The peaks indicate the presence of an ordered B2 phase. Only Phase 1 and Phase 2 are present in high enough volume fractions to produce XRD peaks of the observed intensities. The composition of the (Hf,Ru)-rich Phase 1 is consistent with a HfRu–B2 phase; while Nb and Ru can potentially form an ordered B2 phase, the (Mo,Nb)-rich phase contains only 4.5 at. pct Ru. This is significantly below the composition necessary for ordering in the Nb–Ru binary-phase diagram (~40 at. pct).^[38] Therefore, Phase 1 is identified as an ordered HfRu–B2 phase. Phase 2 is composed primarily of Nb with significant additions of Mo (22.3 at. pct) and Hf

(15.1 at. pct); both elements have large solubilities in disordered BCC Nb.^[51,53] Phase 2 is, therefore, tentatively identified as a disordered BCC phase. Given the shared peaks are insufficiently separated to allow calculation of both experimental lattice parameters, the lattice parameter of the B2 phase is derived only from the 1st, 3rd, and 5th peaks, and the calculated lattice parameter of the remaining peaks is reported separately in Table II as BCC/B2. Phase 3 and Phase 4 were not identified.

Corresponding compositions for the four identified phases are recorded in Table III, along with the composition of the BCC + B2 nanoparticle regions. The compositions of the B2 grains and the BCC + B2 nanoparticle regions were also measured by EPMA and are reported in Table IV.

3. $Hf_{25}Mo_{25}Ta_{25}Ru_{25}$

$Hf_{25}Mo_{25}Ta_{25}Ru_{25}$ is composed primarily of a single-near-equimolar (22.9 at. pct Hf, 23.0 at. pct Mo, 28.7 at. pct Ta, and 25.4 at. pct Ru) Phase 1 (Figure 6). The segregation present in Phase 1 is dendritic in appearance, with the inter-dendritic regions enriched slightly in Hf and Ru, and the dendrite cores enriched slightly in Mo and Ta (Table III). The grain boundaries are Hf enriched with three distinct Hf-rich phases: a phase exhibiting solidification segregation (referred to as Phase 2), a phase darker in backscatter electron contrast and composed of primarily Hf (84 at. pct, referred to as Phase 3) and a bright phase enriched in Hf, O, and less than 3 at. pct Mo + Ru (referred to as Phase 4). Phase 2 exhibits areas enriched in Hf and others enriched in Mo and Ta; Ru is distributed evenly throughout the phase. Pores are also preferentially located in the intergranular regions. At the border of the intergranular region, Phase 1 exhibits a significant enrichment of Hf (45.7 at. pct) and Ru (27.3 at. pct), and a depletion of Mo and Ta. HfO_2 particles of similar composition and high O content to those observed in $Hf_{33}Mo_{34}Ru_{33}$ are also present with varying sizes and locations. Phases 3 and 4 contain significantly less O than the HfO_2 particles. Corresponding compositions for the four identified phases are recorded in Table III.

An XRD scan of the alloy is presented in Figure 2. A single set of peaks is present, which is indicative of an ordered B2 phase (with a peak missing for the (111) reflections). Phase 1 contains large amounts of Ru, which is the necessary component to form the B2 phase, indicating that it is the source of the B2 reflections.^[37,39] However, approximately one micron from the edge of the intergranular regions' nano-scale height variations can be observed in the SE images of Phase 1, indicating potential phase decomposition within the near-equimolar region that affects polishing behavior. Further evidence for the decomposition of Phase 1 into BCC and B2 regions requires further TEM analysis.

4. $Hf_{20}Mo_{20}Nb_{20}Ta_{20}Ru_{20}$

$Hf_{20}Mo_{20}Nb_{20}Ta_{20}Ru_{20}$ exhibits an apparent cored peritectic microstructure, with dark (Mo,Ta)-rich Phase 1 dendrites surrounded by a (Hf, Ru)-rich Phase 2 (Figures 7(a) and (c)). The Phase 2 rings are irregular

Table III. Identified Phases, Assigned Crystal Structures, and Their Compositions (At. Pct) as Measured by EDS of the As-Cast Alloys

Alloy	Region	Crystal Structure	Hf	Mo	Nb	Ru	Ta	W
Mo ₂₅ Nb ₂₅ Ta ₂₅ Ru ₂₅	inter-dendritic region	B2	—	12.7 to 23.7	18.1 to 36.2	21.9 to 33.3	10.3 to 27.7	—
	intra-dendritic region	B2	—	15.8 to 30.5	15.3 to 25.2	12.7 to 29.0	17.5 to 30.5	—
	inter-dendritic region	BCC	—	15.5 to 23.1	15.6 to 21.7	16.1 to 30.2	20.4 to 26.6	10.7 to 23.7
Mo ₂₀ Nb ₂₀ Ta ₂₀ Ru ₂₀ W ₂₀	intra-dendritic region	BCC	—	19.1 to 26.0	11.6 to 18.6	9.8 to 22.4	17.8 to 25.5	16.9 to 31.7
	Phase 1	B2	51.0	3.3	—	45.7	—	—
Hf ₃₃ Mo ₃₄ Ru ₃₃	Phase 2	BCC	*	*	—	*	—	—
	Phase 3	σ	4.8	47.9	—	47.4	—	—
	lamellar B2 + BCC	B2 + BCC	21.6	57.3	—	21.1	—	—
	nanoparticle B2 + BCC	B2 + BCC	7.5	83.4	—	9.1	—	—
Hf ₂₅ Mo ₂₅ Nb ₂₅ Ru ₂₅	Phase 1	B2	43.0	7.0	9.7	40.3	—	—
	Phase 2	BCC	15.1	22.3	58.1	4.5	—	—
	Phase 3	—	74.3	5.5	19.5	0.7	—	—
	Phase 4	—	38.0	11.0	49.6	1.4	—	—
Hf ₂₅ Mo ₂₅ Ta ₂₅ Ru ₂₅	nanoparticle B2 + BCC	B2 + BCC	17.4	24.5	49.7	8.4	—	—
	Phase 1, inter-dendritic region	—	22.7 to 26.8	19.9 to 23.4	—	24.0 to 29.5	24.4 to 30.0	—
	Phase 1, intra-dendritic region	—	20.1 to 25.2	20.9 to 25.3	—	23.0 to 27.8	26.8 to 31.2	—
	Phase 2	—	47.7	24.0	—	10.1	17.9	—
Hf ₂₀ Mo ₂₀ Nb ₂₀ Ta ₂₀ Ru ₂₀	Phase 3	—	84.0	5.0	—	3.4	7.6	—
	Phase 4	—	94.7	0.9	—	0.5	3.9	—
	Phase 1	BCC	10.4	29.1	20.2	10.6	29.5	—
	Phase 2	B2	43.8	4.6	7.4	38.7	5.5	—
Hf ₂₅ Nb ₂₅ Ru ₂₅ W ₂₅	Phase 3	—	24.2 to 40.0	9.1 to 16.8	28.0 to 35.5	5.7 to 9.8	9.6 to 20.5	—
	Phase 4	—	82.1	2.2	9.4	1.0	5.4	—
	nanoparticle B2 + BCC (last liquid)	B2 + BCC	14.6	25.3	21.1	12.8	26.3	—
	nanoparticle B2 + BCC (dendrite core)	B2 + BCC	18.8	19.9	29.4	10.3	21.7	—
Hf ₂₅ Nb ₂₅ Ru ₂₅ W ₂₅	Phase 1, interdendritic region	BCC	4.2 to 15.2	—	28.2 to 58.6	2.4 to 9.8	—	16.8 to 64.6
	Phase 1, intra-dendritic region	BCC	0.0 to 9.7	—	18.6 to 42.1	0.0 to 7.4	—	43.1 to 77.2
	Phase 1	B2	45.5	—	6.4	45.6	—	2.4
	nanoparticle B2 + BCC	BCC	17.2	—	57.8	8.3	—	16.8

Error is on the order of a few at. pct percent

*Regions too small to evaluate by EDS

and broken up by another phase consistent in backscatter electron contrast with Phase 1, yielding an irregular 'cobblestone' appearance. Outside the Phase 2 rings are regions of a third phase (Phase 3) significantly enriched in Nb and Hf and depleted in Mo and Ta. Segregation is present within Phase 3, with variations in composition resulting in brighter Hf-enriched regions (reaching 40 at. pct Hf) and darker (Mo, Ta)-rich regions (\approx 15 to 20 at. pct Mo/Ta); Nb and Ru content vary slightly. Nano-scale precipitates present within Phase 1 and Phase 3 regions are consistent in backscatter electron contrast and preferential polishing behavior in SE images with Phase 2. Within the Phase 1 dendrites, the location of the nanoparticles is consistent with regions enriched in Hf and Ru; a compositional linescan is presented in Figures 5(c) and (d), demonstrating the disappearance of the nanoparticles with increasing Mo and Ta content. Outside of the nanoparticle regions, there is little segregation within the dendrite cores. In contrast, while nanoparticles are nearly always present in Phase 3, the nanoparticles appear with decreasing Hf content and increasing Mo and Ta content. Some of the nanoparticles appear coarsened in chain-like arrangements.

Within Phase 3, there is another minor phase concentrated in the Hf-rich regions. This is noted as Phase 4; it has a bright white contrast in BSE images and is composed of 82 at. pct Hf. This phase contains comparable O content to Phase 1. A fifth minor phase rich in Hf and O and containing internal striations in BSE images is identified as HfO_2 , consistent with the previous alloys.

The peritectic Phase 1 and Phase 2 microstructure is not uniform throughout the ingot, with some regions demonstrating incomplete rings of Phase 2 (7(b) and (a)). In these regions, all Phase 1 regions contain nano-scale precipitates of Phase 2, excepting the areas directly adjacent to the larger Phase 2 grains. The bulk composition does not change between these regions.

A XRD scan of the alloy is presented in Figure 2. One set of peaks is visible, demonstrating reflections consistent with an ordered B2 phase; however, slight shouldering is visible in the (110), (200), and (211) reflections. Similar to previous alloys, the (Hf,Ru) content of the Phase 2 grains is consistent with an ordered HfRu-B2 phase, and Phase 2 is, therefore, identified as an ordered B2 phase. Phase 1 is composed of large amounts of Mo and Ta, which form a disordered BCC phase, and insufficient Ru is present to result in ordering, indicating that Phase 1 is likely a disordered BCC phase. Similar to $\text{Hf}_{25}\text{Mo}_{25}\text{Nb}_{25}\text{Ru}_{25}$, the lattice parameter of the B2 phase is derived only from the 1st, 3rd, and 5th peaks and the calculated lattice parameter of the remaining peaks is reported separately in Table II as BCC/B2. The crystal structures of Phases 3 and 4 are not identified.

Corresponding compositions for the four identified phases are recorded in Table III, along with the composition of the BCC + B2 nanoparticle regions. The compositions of the B2 grains and the BCC + B2 nanoparticle regions were also measured by EPMA (Table IV).

5. $\text{Hf}_{25}\text{Nb}_{25}\text{Ru}_{25}\text{W}_{25}$

$\text{Hf}_{25}\text{Nb}_{25}\text{Ru}_{25}\text{W}_{25}$ demonstrates significant dendritic segregation (Figure 8), with the formation of highly W-rich dendrite cores (composed of 65 to 78 at. pct W) and inter-dendritic regions enriched in Nb (28 to 59 at. pct), Hf (4 to 15 at. pct), and Ru (2 to 10 at. pct). Within the inter-dendritic regions are larger grains of a (Hf,Ru)-rich phase. The dendritic matrix phase is defined as Phase 1 and the (Hf,Ru)-rich phase is referred to as Phase 2. Phase 2 is present in multiple morphologies: (i) large continuous regions' tens of microns across, (ii) nano-scale "feathery" regions that alternate with Phase 2 and which coarsen from a core towards the edges, and (iii) nano-scale precipitates embedded in the inter-dendritic regions. While the nanoparticles cannot be compositionally measured by EDS due to their size, the similarity in backscatter electron contrast and preferential polishing behavior indicate that the nanoparticles are the same phase as the larger (Hf, Ru)-rich grains and particles. In some regions, the appearance of nanoparticles follows a compositional trend (Figures 5(e) and (f)); their presence is associated with decreasing W content and increasing Nb, Hf, and Ru content. Channeling contrast and particle coarsening consistent with sub-grain or grain boundaries are also visible in Nb-rich inter-dendritic regions. Near the edges of the ingot, the dendritic morphology is less apparent and the Phase 2 regions are more globular in appearance and aligned towards the center of the ingot. Here the highly W-enriched Phase 1 regions do exhibit the formation of small nanoparticles, with slightly coarser particles in the (Nb,Ru)-enriched regions. A small area fraction of a third phase bright in backscatter electron contrast was observed but was found in sizes too small to evaluate with EDS. HfO_2 particles similar in oxygen content and composition as those observed in the other alloys are also present with varying sizes and locations.

The XRD scan associated with this alloy demonstrates two sets of peaks: one set of peaks consistent with an ordered B2 phase, and a second set consistent with a disordered BCC phase (Figure 2). The calculated lattice parameters are reported in Table II. The disordered BCC peaks are smaller than the B2 peaks and shifted slightly to higher 2θ , indicating the BCC phase has a smaller lattice parameter than the B2 phase. W does not form a B2 phase in the W-Ru binary^[54] and the Ru concentrations in the inter- and intra-dendritic regions of Phase 1 are \leq 10 at. pct, which is insufficient for ordering in the NbRu phase diagram.^[38] Therefore, the (Hf,Ru)-rich Phase 2 is identified as the ordered B2 phase, consistent with previous alloys, and the dendritic (Nb, W)-rich Phase 1 is tentatively identified as a disordered BCC phase. Using the experimental lattice parameters, the two phases would have a misfit of 0.75 pct.

Corresponding compositions for the three identified phases are recorded in Table III, along with the composition of the BCC + B2 nanoparticle regions. The composition of the B2 grains was also measured by EPMA (presented in Table IV).

Table IV. Identified Phases in the As-Cast Alloys and Their Compositions (At. Pct) as Measured by EPMA

Alloy	Region	Hf	Mo	Nb	Ru	Ta	W
Hf ₃₃ Mo ₃₄ Ru ₃₃	B2	50.0 ± 0.2	3.5 ± 0.2	—	46.5 ± 0.2	—	—
Hf ₂₅ Mo ₂₅ Nb ₂₅ Ru ₂₅	B2	42.6 ± 0.8	6.6 ± 0.8	8.6 ± 0.7	42.3 ± 0.8	—	—
	B2 + BCC	18.4 ± 1.3	18.8 ± 1.1	52.9 ± 2.3	9.7 ± 1.4	—	—
Hf ₂₀ Mo ₂₀ Nb ₂₀ Ta ₂₀ Ru ₂₀	B2	35.0 ± 2.3	8.5 ± 1.4	8.1 ± 1.6	39.2 ± 2.1	9.2 ± 1.5	—
	B2 + BCC	13.7 ± 1.5	24.6 ± 1.8	27.1 ± 1.9	12.3 ± 0.9	22.4 ± 1.4	—
Hf ₂₅ Nb ₂₅ Ru ₂₅ W ₂₅	B2	45.5 ± 0.5	—	5.7 ± 0.5	47.0 ± 0.4	—	1.9 ± 0.5

All reported compositions represent the average of multiple (at least 10) measurements

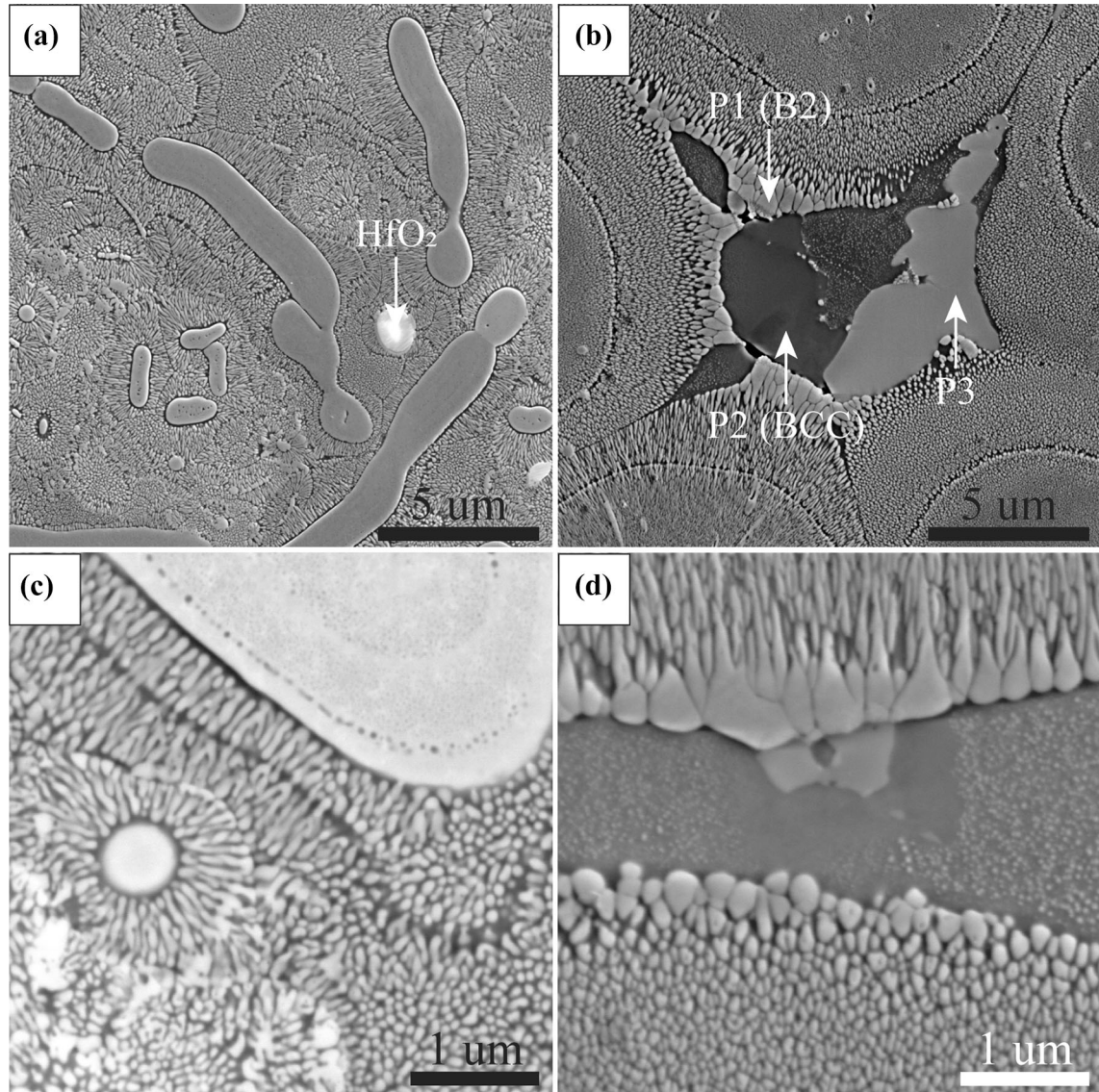
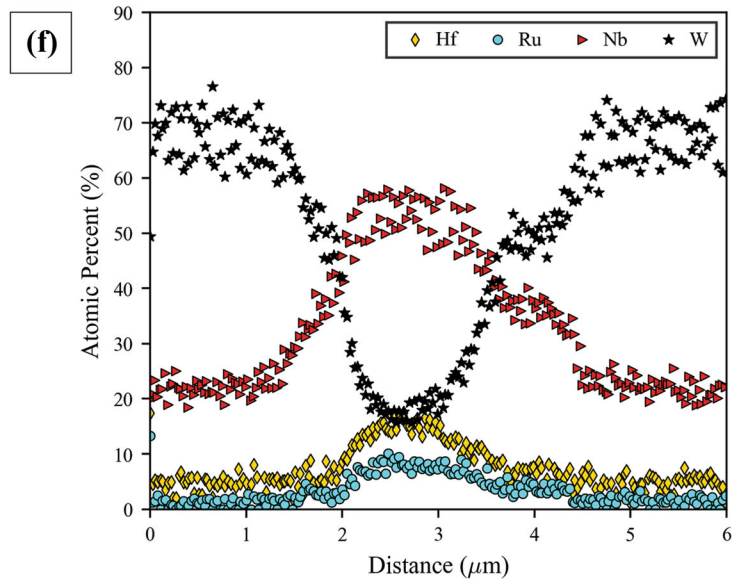
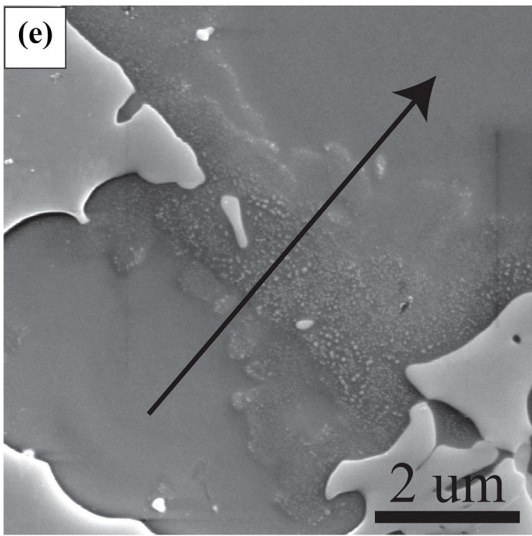
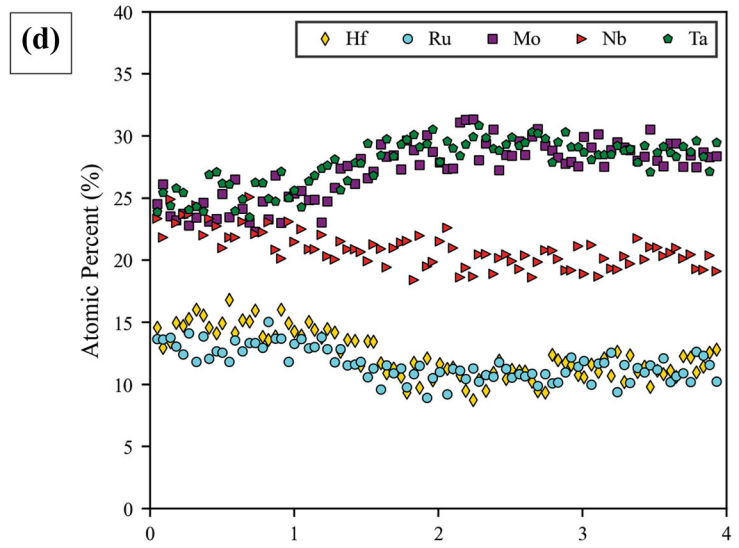
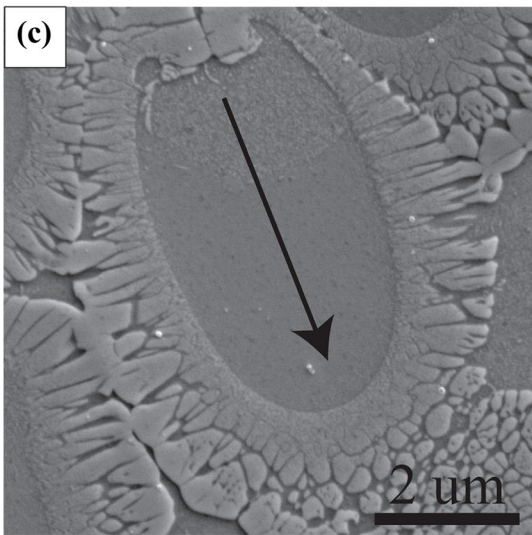
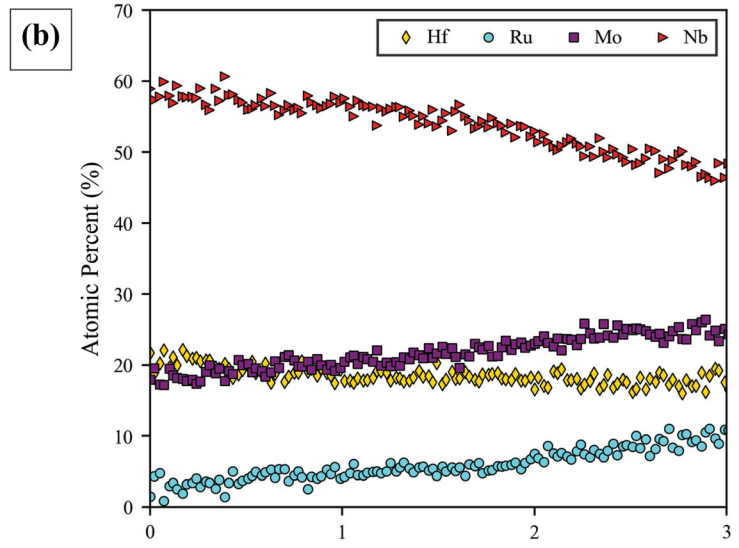
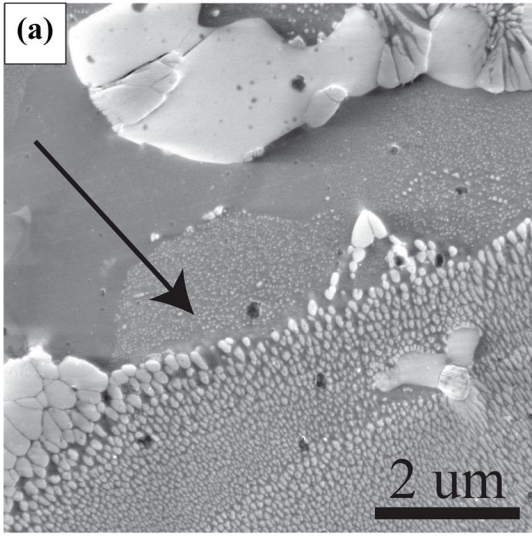


Fig. 4—(a) and (b) SE images of as-cast Hf₂₅Mo₂₅Nb₂₅Ru₂₅. Higher magnification (c) BSE and (d) SE images of the regions shown in (a) and (b), respectively. Four phases are identified. Precipitation of Phase 1 nanoparticles is visible in the Phase 2 regions in (b) and (d). P1 is an ordered HfRu–B2 phase and P2 is a disordered (Mo, Nb)–BCC phase.

C. TEM Analysis of Hf₂₀Mo₂₀Nb₂₀Ta₂₀Ru₂₀

Nano-scale precipitates are visible in four of the seven alloys, all Hf-containing: Hf₃₃Mo₃₄Ru₃₃, Hf₂₅Mo₂₅Nb₂₅Ru₂₅, Hf₂₀Mo₂₀Nb₂₀Ta₂₀Ru₂₀, and Hf₂₅Nb₂₅Ru₂₅W₂₅. These nanoparticles are present both

in the as-cast condition and form in some alloys in the heat-treated conditions (Section III–D). The nanoparticles are consistent in appearance in both BSE and SE images with the B2 phases identified in each alloy and are relatively similar in size across alloys. The nanoparticles consistently appear in Hf- and/or Ru-enriched



◀Fig. 5—(a) BSE micrograph of $\text{Hf}_{25}\text{Mo}_{25}\text{Nb}_{25}\text{Ru}_{25}$ with marker indicating direction of compositional linescan in (b). Nanoparticles occur in region enriched in Mo and Ru. (c) SE micrograph of $\text{Hf}_{20}\text{Mo}_{20}\text{Nb}_{20}\text{Ta}_{20}\text{Ru}_{20}$ with marker indicating direction of EDS linescan in (d). Nanoparticles occur in region enriched in Hf, Nb, and Ru. (e) SE micrograph of $\text{Hf}_{25}\text{Nb}_{25}\text{Ru}_{25}\text{W}_{25}$ with marker indicating direction of EDS linescan in (f). Nanoparticles appear in regions enriched in Hf, Nb, and Ru.

regions. To further characterize the nanoparticles, a TEM foil was lifted out from a region of the as-cast $\text{Hf}_{20}\text{Mo}_{20}\text{Nb}_{20}\text{Ta}_{20}\text{Ru}_{20}$ containing a high density of nanoparticles (the regions presented in Figures 7(b) and (d)).

The low-angle dark-field image in Figure 9(a) shows a collection of coarse (Hf, Ru)-rich B2 grains at the bottom and upper left of the image, and an aligned group of coarsened (Hf,Ru)-rich B2 nanoparticles through the center of the image. The remaining area is occupied by nanoparticles ranging from 50 to 100 nm in diameter embedded in a (Mo, Nb, Ta)-rich BCC phase. The coarsened nanoparticles in the diagonal of the image are rectangular in appearance and can reach up to 150 nm in their longest dimension. Larger nanoparticle-free BCC regions are visible adjacent to the nanoparticle chain and the coarse B2 grains. Overlapping the coarse B2 grains in Figure 9(b) are networks of dislocations with a spacing of 44 ± 5 nm; these dislocation networks are typical of misfit dislocations at a two-phase interface. The Burgers vector of the misfit dislocations was confirmed to be $1/2[111]$ by $\mathbf{g}\cdot\mathbf{b}$ analysis in conventional TEM (Supplemental Table 1).

Lattice parameters of the BCC and B2 phases were calculated from the SAED pattern taken from the BCC + B2 nanoparticle region. The lattice parameters are $a_{\text{BCC}} = 3.27$ Å and $a_{\text{B2}} = 3.29$ Å, resulting in a lattice misfit of 0.61 pct. Further, utilizing the spacing between the dislocations in Figure 9(b) and the following equation:

$$\delta = b/s, \quad [1]$$

where δ is the calculated misfit between the BCC matrix and the coarse B2 grains, b is the magnitude of the BCC $a/2\langle 111 \rangle$ Burgers vector, a is the lattice parameter of the BCC phase derived from TEM, and s is the spacing between the misfit dislocations at the BCC/B2 interface, a misfit of 0.53 ± 0.07 pct can be calculated. This value is consistent with the misfit derived directly from the SAED pattern lattice parameters.

D. Microstructural Evolution After High Temperature Heat Treatment

The alloys were heat treated at 1500 °C ($\text{Hf}_{33}\text{Mo}_{34}\text{Ru}_{33}$) and 1600 °C ($\text{Hf}_{25}\text{Mo}_{25}\text{Nb}_{25}\text{Ru}_{25}$, $\text{Hf}_{25}\text{Mo}_{25}\text{Ta}_{25}\text{Ru}_{25}$, $\text{Hf}_{20}\text{Mo}_{20}\text{Nb}_{20}\text{Ta}_{20}\text{Ru}_{20}$, $\text{Hf}_{25}\text{Nb}_{25}\text{Ru}_{25}\text{W}_{25}$) to investigate the thermal stability of the BCC and B2 phases (Figures 10 and 11). After heat treatment, any structures formerly described in the as-cast samples remain in the heat-treated (HT) microstructures and

demonstrate coarsening and homogenization; the only exception is the decomposition of near-equi-molar region of $\text{Hf}_{25}\text{Mo}_{25}\text{Ta}_{25}\text{Ru}_{25}$ into two phases. Compositions of the observed phases are reported in Table VI. Except for HT- $\text{Hf}_{33}\text{Mo}_{34}\text{Ru}_{33}$, all the coarse B2 phases showed a decrease in Mo, Nb, Ta, and W content and an increase in Hf and Ru. The composition of the $\text{Hf}_{33}\text{Mo}_{34}\text{Ru}_{33}$ HfRu–B2 phases remained constant.

The XRD scans presented in Figure 12 are consistent with the XRD scans from the as-cast samples (Figure 2). Monoclinic HfO_2 peaks are additionally visible in the HT- $\text{Hf}_{25}\text{Mo}_{25}\text{Nb}_{25}\text{Ru}_{25}$ diffraction scan. The lattice parameters are reported in Table V.

Interestingly, in the HT- $\text{Hf}_{33}\text{Mo}_{34}\text{Ru}_{33}$ (Figures 10(a), (c)), significant cracking occurred in the microstructure after heat treatment. Regions of dark BSE contrast in Figure 10(a) show where cracking occurred, with a concentration of cracks at interfaces between the Mo-BCC phase and the HfRu–B2 phase (Figure 10(b)). Coarsening of the B2 nanoparticles embedded in the BCC phase also occurred. The nanoparticles are irregular in shape and size and range from 34 to 404 μm in length along their longest dimension.

In the HT- $\text{Hf}_{25}\text{Mo}_{25}\text{Nb}_{25}\text{Ru}_{25}$ (Figures 10(c) and (d)), the segregation in the intergranular BCC phases has been eliminated, and the pre-existing nanoparticles have coarsened to 60 to 400 nm in diameter. They are still spherical in appearance. The larger B2 grains at the border of the intergranular and intragranular regions further coarsened to form a continuous layer of the B2 phase. Similarly, coarsening of the “feathered” B2 within the grains resulted in a continuous network of the B2 phase with embedded BCC regions. Phases 3 and 4 were present in very small volume fractions ($a_f < 0.01$) and could not be evaluated for their compositions.

In the HT- $\text{Hf}_{25}\text{Mo}_{25}\text{Ta}_{25}\text{Ru}_{25}$ (Figures 10(e) and (f)), the near-equi-molar (Hf, Mo, Ta, Ru)-rich regions have decomposed into two phases: Phase 1 and Phase 5. Phase 1 is more resistant to polishing and demonstrates slightly lighter backscatter electron contrast compared to Phase 5. The phases are too small in the core of the grains to measure their compositions with EDS, but Phase 1 coarsens sufficiently towards the grain boundaries to measure an average composition of 47.0 at. pct Hf and 39.2 at. pct Ru. Consistent with the other alloys, Phase 1 is, therefore, identified as a HfRu–B2 phase. Phase 5 is tentatively identified as a disordered BCC phase rich in Mo and Ta, though further investigation is required. The low Mo and Ta content of the measured B2 grains would necessarily require the rejection of Mo and Ta to the surrounding phase and in the other Hf-containing alloys the Mo-, Nb-, Ta-, and W-rich phases have all been disordered BCC. All three Hf-rich phases identified in the as-cast sample (Section III–B–3) remain after heat treatment. Phase 2 experienced a significant reduction in Hf content from 47.7 to 27.3 at. pct and an enrichment of Mo (+10.9 at. pct) and Ta (+10.8 at. pct); it is no longer composed primarily of Hf. The Ru content decreased only by 1.5 at. pct. Nanoparticles with similar backscatter and polishing behavior as the coarse B2 grains precipitated within

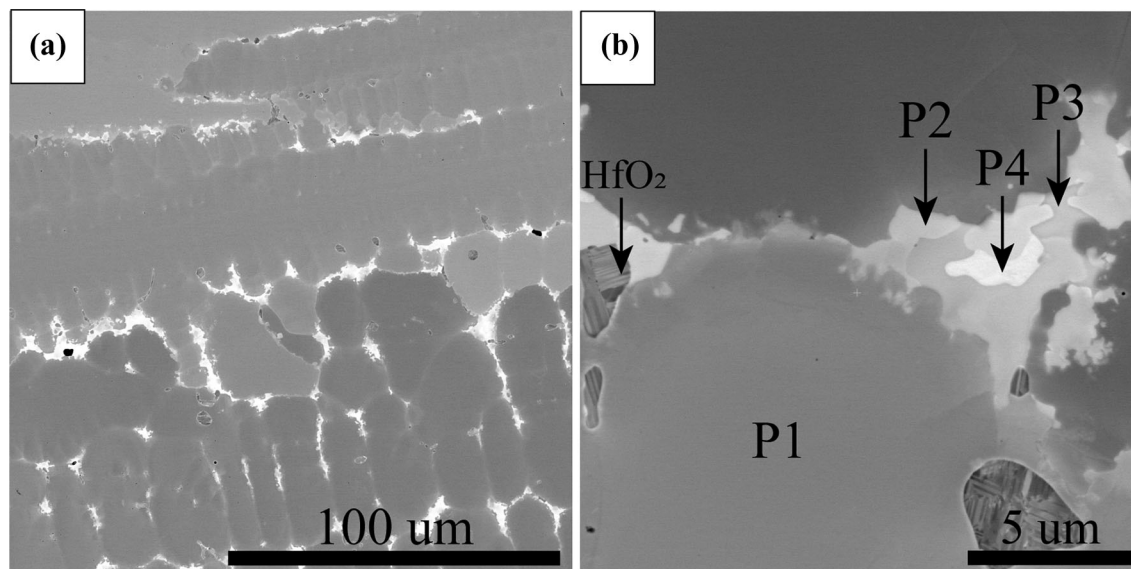


Fig. 6—(a) and (b) BSE images of as-cast $\text{Hf}_{25}\text{Mo}_{25}\text{Ta}_{25}\text{Ru}_{25}$. Five phases are identified, with three of them occupying the intergranular region.

Phase 2 regions in small quantities. These two-phase regions are too small to measure with EDS.

In the HT- $\text{Hf}_{20}\text{Mo}_{20}\text{Nb}_{20}\text{Ta}_{20}\text{Ru}_{20}$ (Figures 11(a) through (c)), new HfRu-B2 nanoparticles precipitated throughout the formerly single-phase BCC dendrite cores. The nanoparticles are uniformly dispersed throughout the cores and appear spherical in shape, with an area fraction of 0.29 ± 0.09 . The particles range in size from 30 to 100 nm in diameter. The nanoparticles that formed prior to heat treatment exhibit coarsening from 50 to 100 to 70 to 500 nm in size along their longest dimension, with the particles in the Hf-enriched zones coarsening faster than the particles in the peritectic cores. EDS measurements of sufficiently large BCC regions indicate that the BCC phase is depleted of Hf and Ru compared to the BCC phase formerly present within the peritectic cores and inter-peritectic regions in the as-cast regions, with the combined quantity of Hf + Ru reducing to ≈ 10 at. pct.

In the HT- $\text{Hf}_{25}\text{Nb}_{25}\text{Ru}_{25}\text{W}_{25}$ (Figures 11(d) through (f)), the dendritic segregation in the disordered (Nb, W)-rich BCC phase remains. Coarsening of the pre-existing nanoparticles is also observed. Similar to HT- $\text{Hf}_{20}\text{Mo}_{20}\text{Nb}_{20}\text{Ta}_{20}\text{Ru}_{20}$, new nanoparticles have precipitated in the Nb-rich intra-dendritic regions and in between the HfRu-B2 grains (Figures 11(e) and (f)). The heat treatment also resulted in the formation of two new two-phase regions in the highly W-enriched dendrite cores (≈ 65 to 73 at. pct W): irregular B2 lamellae (with an average Ru content of at 2.5 pct) and regions with a “fuzzy” appearance (with an average Ru content of 1.6 at. pct). Regions directly adjacent to those morphologies but which contain no evidence of particles are completely depleted of Ru (0 at. pct Ru) and contain only small amounts of Hf (≤ 3 at. pct Hf).

E. Micropillar Compression

of HT- $\text{Hf}_{20}\text{Mo}_{20}\text{Nb}_{20}\text{Ta}_{20}\text{Ru}_{20}$ Nanoparticle Regions

To investigate the mechanical behavior of new BCC + B2 nanoparticle microstructures, targeted regions in the HT- $\text{Hf}_{20}\text{Mo}_{20}\text{Nb}_{20}\text{Ta}_{20}\text{Ru}_{20}$ material were identified for micropillar compression experiments. Micropillars were fabricated towards the center of the dendrite cores in order to avoid the influence of grain boundaries and variations in precipitate morphology. The compression axis (Z) crystal direction for each micropillar is shown in the inset of Figure 13(a).

The engineering stress-strain curves (Figure 13(a)) exhibit high 0.2 pct offset yield strengths of 1250, 1630, 1770, and 1835 MPa, respectively. These values correspond to critical resolved shear stresses of 616, 810, 830, and 917 MPa, assuming that the deformation is accommodated on the maximum resolved shear-stress (MRSS) plane. The MRSS planes are noted for each pillar in Figure 13 and the yield strength, resolved shear strengths, and modulus of each pillar are reported in Table VII. Slip traces on the surface of each deformed micropillar (Figures 13(b) through (e)) are consistent with deformation on the MRSS plane. Pillars oriented for glide along the $(10\bar{1})$, $(01\bar{2})$, and (143) planes exhibited additional slip traces corresponding to secondary highly stressed slip systems. All pillars exhibited signs of cross-slip, though due to the presence of the nanoparticles, identification of cross-slip traces on the surface of the pillars could not be accurately performed. The influence of size effects on the yield strengths measured in these experiments was estimated using the single-arm source model of Parthasarathy *et al.*^[55] Using a shear modulus determined as a rule of mixtures for the pure elements,^[56–58] the pillar size contributed approximately 23 MPa to the yield strength, which is less than 2 pct of the smallest value measured.

An electron transparent sample was prepared from the deformed pillar oriented for glide on the (312) plane (Figures 13(d) and 14) such that the foil normal was close to the glide plane. This pillar was the only sample tested oriented in a “single slip” orientation, thus, likely to contain dislocations of predominately a single burgers vector. The sample was single crystalline and contained a relatively uniform distribution of B2 nanoparticles on the surface (Figure 13(d)). ADF STEM images of the sample (Figures 14(d) and (f)) show two regions with dense B2 nanoparticle precipitates and a high density of dislocations. Many dislocations appear in paired configurations, likely a result of cooperative shearing of the B2 precipitates by APB-coupled dislocations. Many dislocations have formed Orowan loops, suggesting a

combined shearing and looping behavior. A conventional dark-field (DF) TEM image of the top region of the micropillar shows the high density of B2 nanoparticles alongside numerous dislocations (Figure 14(c)). The precipitates in this sample range from ≈ 43 to 75 nm in diameter. A $\mathbf{g} \cdot \mathbf{b}$ analysis (Table VIII) was performed in conventional TEM, and the Burgers vector direction was determined to be $1/2[\bar{1}11]$ for the dislocations examined. This Burgers vector and surface trace agree with the corresponding slip system with the highest Schmid factor for this pillar, $(312)[\bar{1}11]$, $m = 0.47$.

Trace analysis was performed on ADF STEM images collected at several two-beam tilt conditions to determine the line direction of the dislocation segments

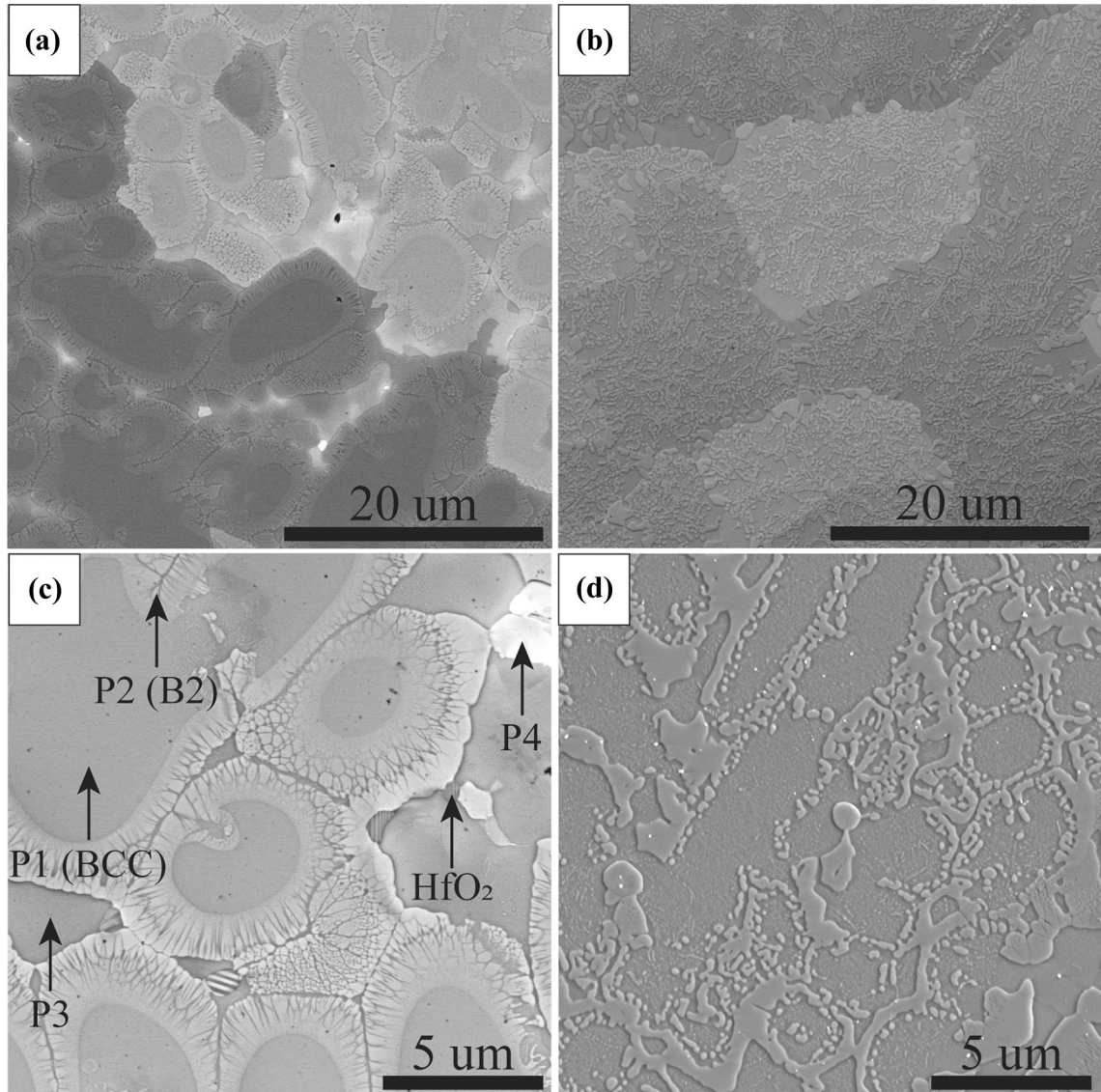


Fig. 7—(a) and (c) BSE images of a peritectic solidification zone in as-cast $\text{Hf}_{20}\text{Mo}_{20}\text{Nb}_{20}\text{Ta}_{20}\text{Ru}_{20}$. (b) and (d) SE images of a different region from (a) and (c) where the ring structure is incomplete. Five phases are identified and present throughout the sample. Precipitation of Phase 1 nanoparticles is visible throughout the Phase 2 regions in (d) and in some locations in (c). P1 is a disordered (Mo)-BCC phase and P2 is an ordered HfRu-B2 phase.

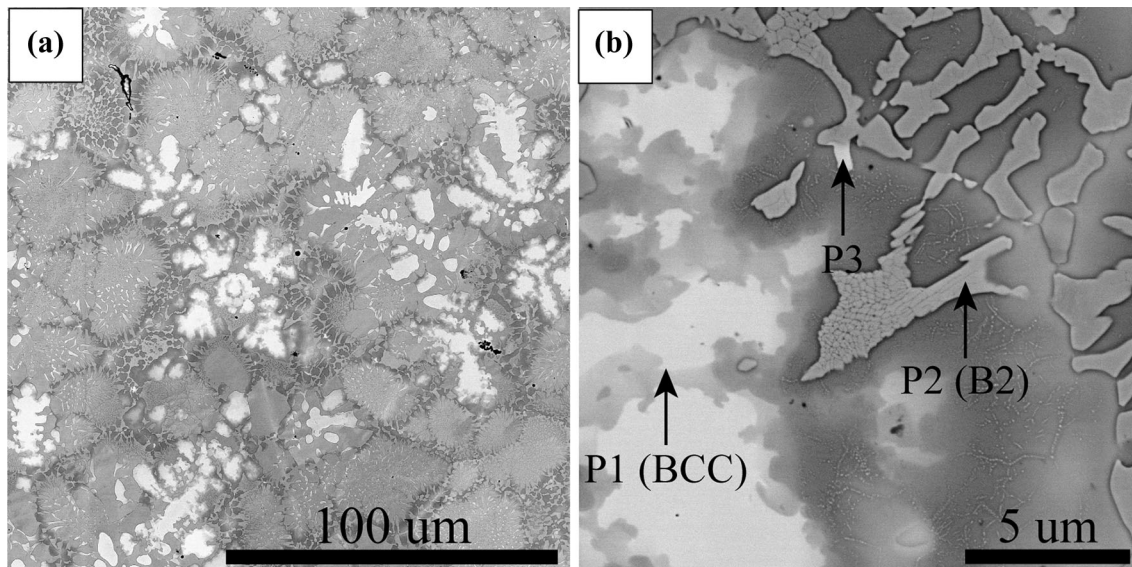


Fig. 8—(a) and (b) BSE images of as-cast $\text{Hf}_{25}\text{Nb}_{25}\text{Ru}_{25}\text{W}_{25}$. Three phases are identified and present throughout the sample. Nanoparticles are visible in the regions of Phase 2 demonstrating darker chemical contrast. P1 is a disordered (Nb, W)-BCC phase and P2 is an ordered HfRu -B2 phase.

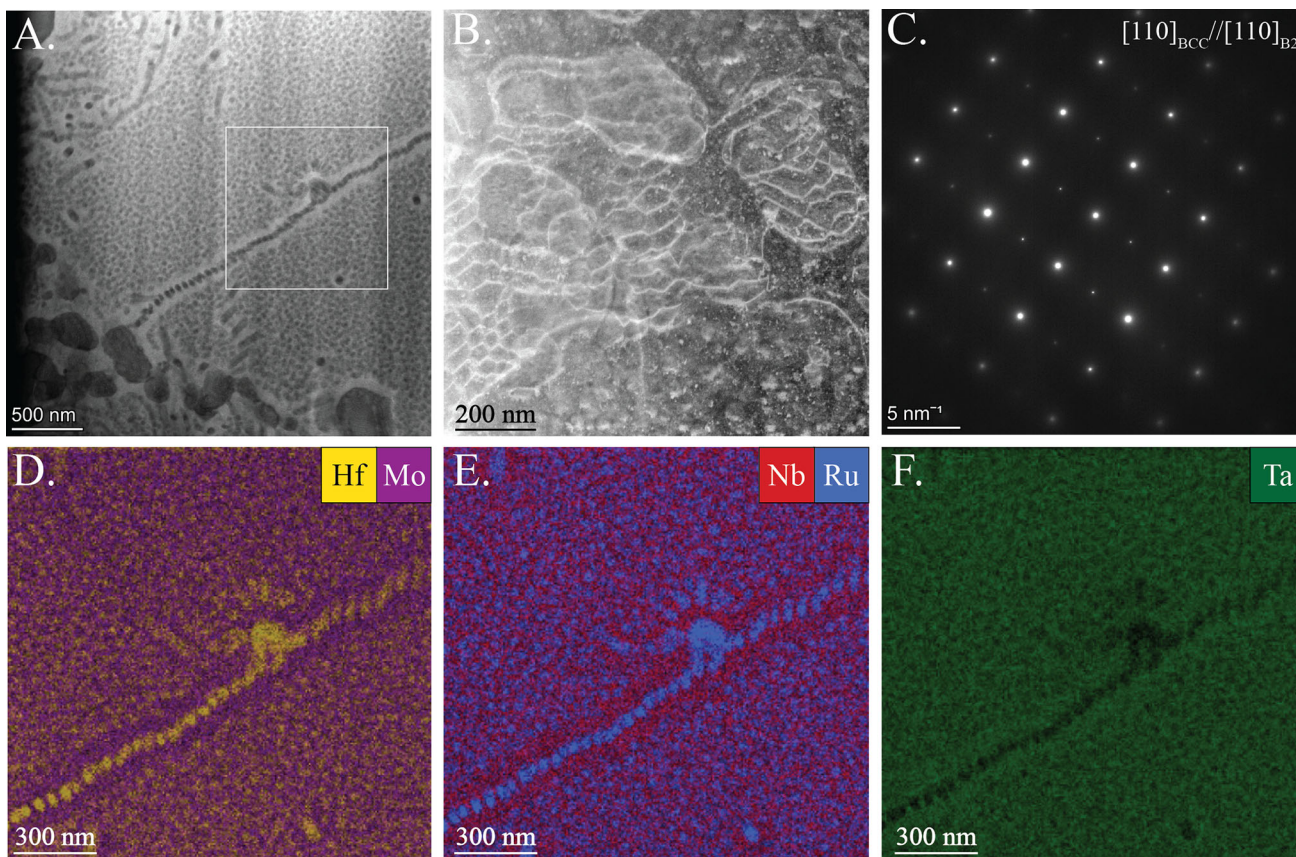


Fig. 9—TEM analysis of a nanoparticle dense region in as-cast $\text{Hf}_{20}\text{Mo}_{20}\text{Nb}_{20}\text{Ta}_{20}\text{Ru}_{20}$. (a) STEM image taken in two-beam condition from a low-angle dark-field detector. Condition was chosen to maximize phase contrast between BCC and B2. (b) A higher magnification HAADF-STEM image of dislocation cells present at a BCC-B2 interface within the foil, visible at the lower left corner in (a). (c) SAED pattern acquired from the nanoparticle + matrix array on the $[110]_{\text{BCC}}$ zone axis, indicating BCC ordering with a B2 superlattice. No additional Heusler ($L2_1$) reflections are visible. (d) through (f). STEM-EDS maps of area marked in (a), showing enrichment of Hf and Ru in the nanoparticles and depletion of Mo, Nb, and Ta.

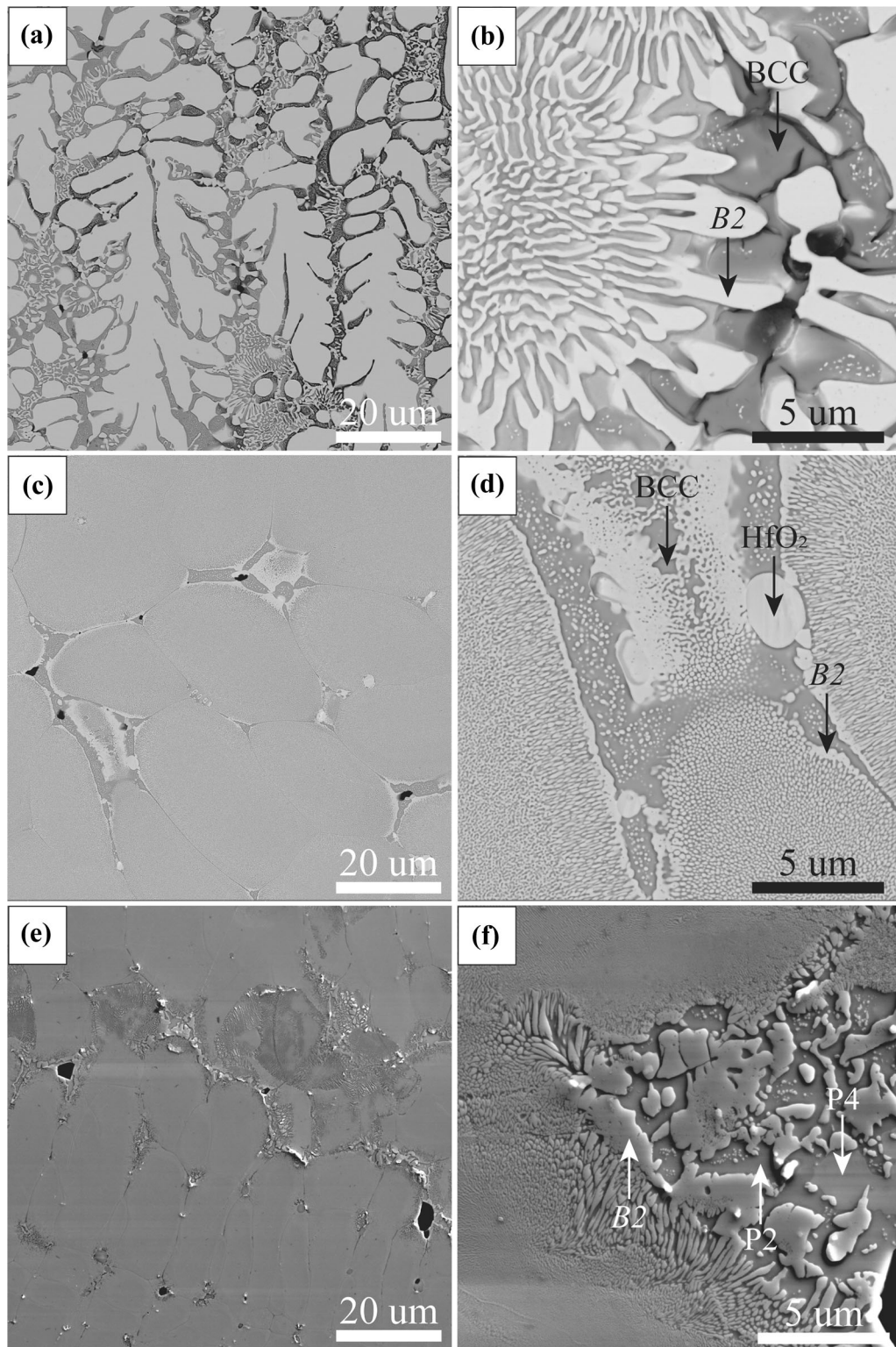


Fig. 10—Microstructure images of alloys after heat treatment at 1500 °C ($\text{Hf}_{33}\text{Mo}_{34}\text{Ru}_{33}$) and 1600 °C ($\text{Hf}_{25}\text{Mo}_{25}\text{Nb}_{25}\text{Ru}_{25}$ and $\text{Hf}_{25}\text{Mo}_{25}\text{Ta}_{25}\text{Ru}_{25}$) for 40 h. (a) and (b) BSE images of $\text{Hf}_{33}\text{Mo}_{34}\text{Ru}_{33}$. Areas with cracking visible exhibit dark contrast in (a). (c) and (d). BSE images of $\text{Hf}_{25}\text{Mo}_{25}\text{Nb}_{25}\text{Ru}_{25}$. Larger BCC regions are visible at grain boundaries. (e) and (f). SE images of $\text{Hf}_{25}\text{Mo}_{25}\text{Ta}_{25}\text{Ru}_{25}$.

(Figure 14(e)). Three segments of a single dislocation were used for this analysis: one nearly screw orientation segment and two mixed/edge-like segments. The nearly screw-character segment (segment 1) has an average line

direction of $[-1.7, 2.3, 1.6]$, which is less than 10 degrees from perfect screw orientation. The shorter segments have line directions of $[1.83, 0.23, -2.65]$ (segment 2) and $[1, 1.85, -2.45]$ (segment 3), which are ≈ 40 and 74

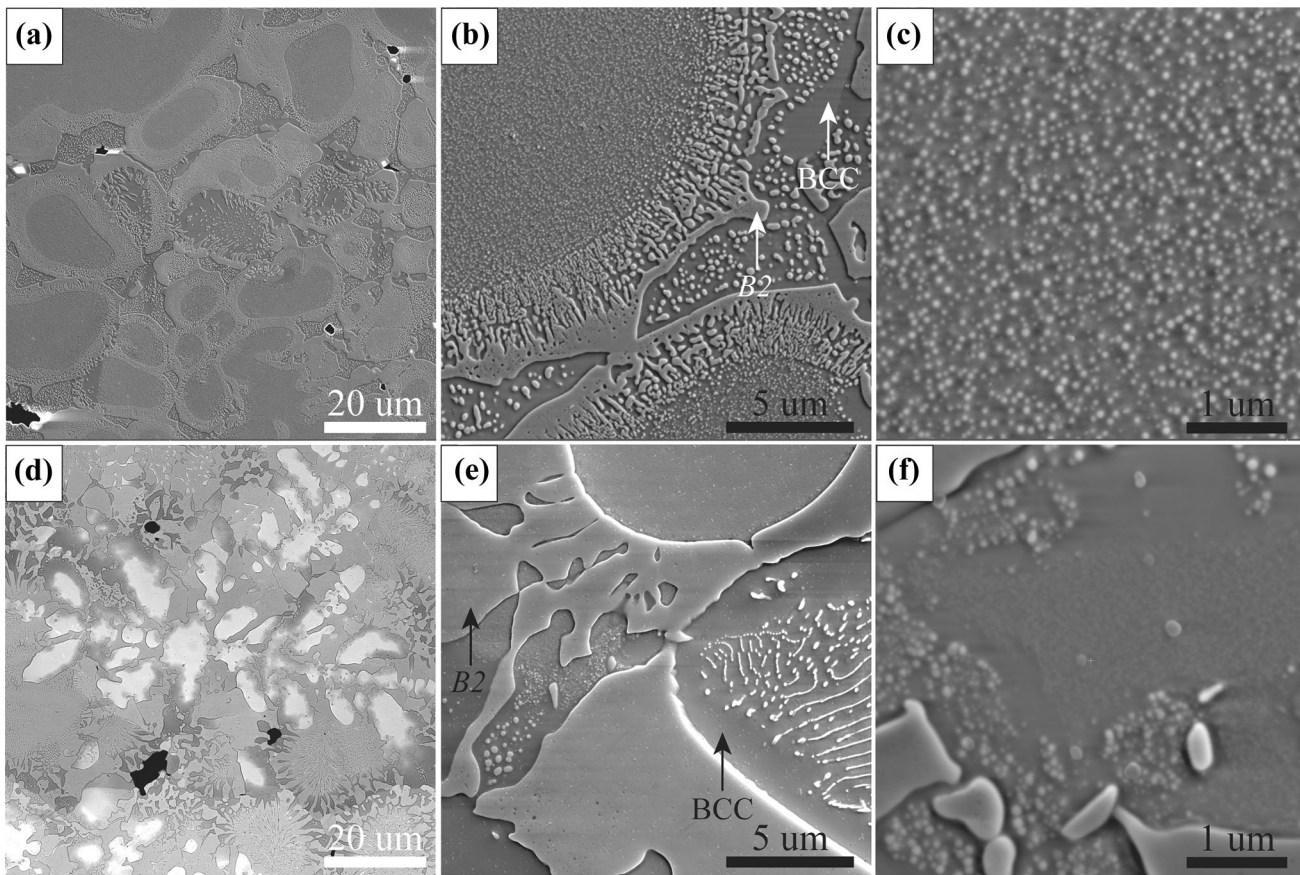


Fig. 11—Microstructure images of $\text{Hf}_{20}\text{Mo}_{20}\text{Nb}_{20}\text{Ta}_{20}\text{Ru}_{20}$ and $\text{Hf}_{25}\text{Nb}_{25}\text{Ru}_{25}\text{W}_{25}$ after 40 h at 1600 °C. (a) through (c). SE images of $\text{Hf}_{20}\text{Mo}_{20}\text{Nb}_{20}\text{Ta}_{20}\text{Ru}_{20}$. Nanoparticle precipitation can be observed throughout the dendrite cores and is magnified in (c). (d) BSE and (e) and (f) SE images of $\text{Hf}_{25}\text{Nb}_{25}\text{Ru}_{25}\text{W}_{25}$. Precipitation of nano-scale features can be observed between the B2 grains in (e), and in the W-rich dendrite cores in (e) and (f).

deg from perfect screw orientation. The error associated with each of these line direction determinations is less than 10 deg. The glide plane was determined by taking the cross product of the two short segments and the Burgers vector ($[\bar{1}11]$). The glide planes determined using this method were (2.9, 0.8, 2) and (2.97, 1, 1.97), both of which agree well with the surface trace and MRSS of (312).

IV. DISCUSSION

Ru additions present an opportunity for design of high temperature BCC + B2 precipitation-strengthened systems in the high-dimensional refractory composition space. The HfRu–B2 phases in the investigated alloys are stable to at least 1600 °C and nano-scale precipitate regions suggest targeted compositions that could be solution and aged. The individual alloy solidification behaviors, trends in the phase compositions, and dislocation interactions with the HfRu–B2 particles are discussed in the following sections. Finally, the possibilities of alloy design utilizing HfRu–B2 particles are discussed.

A. Solidification Behavior of the As-Cast Alloys

Understanding the solidification behavior of each alloy can provide insight for future alloying strategies. Controlling the solidification pathway is important for reducing segregation that can lead to casting defects and developing microstructures with improved mechanical properties. Further, segregation of alloying agents can result in varying phase formation behavior along the solidification path that can suggest new, more optimal compositions.

In the absence of Hf, $\text{Mo}_{25}\text{Nb}_{25}\text{Ta}_{25}\text{Ru}_{25}$ and $\text{Mo}_{25}\text{Nb}_{25}\text{Ta}_{25}\text{Ru}_{20}\text{W}_{20}$ solidify as single-phase dendritic alloys. In both cases, there is segregation of the highest melting point element (W or Ta) to the intra-dendritic regions, along with Mo, and segregation of Nb and Ru to the inter-dendritic region. From this investigation, it is unknown if the B2 ordering of the $\text{Mo}_{25}\text{Nb}_{25}\text{Ta}_{25}\text{Ru}_{25}$ alloy persists until melting. The closest equivalent phases, the NbRu and TaRu B2 phases, are indicated to persist to very high temperatures in their binary-phase diagrams at Ru contents above 40 at. pct, but that is much greater than the amount of Ru present in $\text{Mo}_{25}\text{Nb}_{25}\text{Ta}_{25}\text{Ru}_{25}$.^[38,53,59] It is possible that there is an ordering transition at elevated

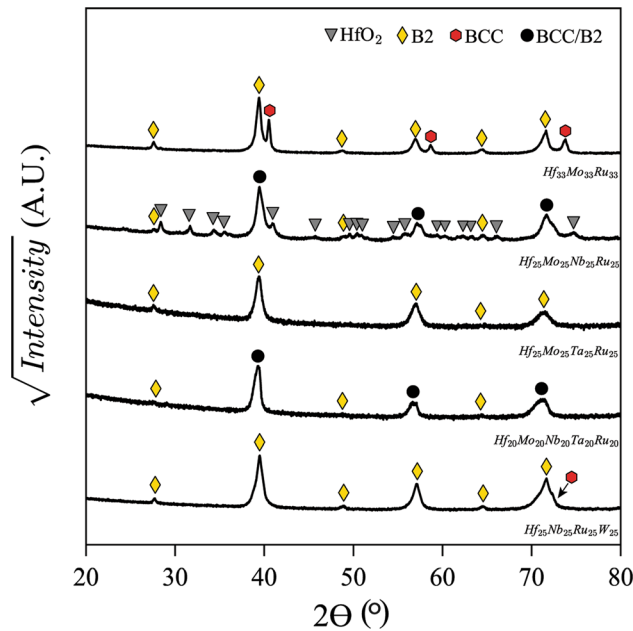


Fig. 12—XRD scans of the heat-treated alloys. $\text{Hf}_{33}\text{Mo}_{34}\text{Ru}_{33}$ was heat treated at 1500 °C for 40 h. All other alloys were heat treated at 1600 °C for 40 h. Peaks associated with a B2 phase were observed in all alloys. Asymmetry in the observed peaks may be the result of a low misfit between the BCC and B2 phases, causing overlapping peaks, or chemistry and lattice parameter variations within the disordered BCC phases.

temperatures where the alloy becomes disordered; further investigations are required.

The Hf-containing alloys have microstructures indicative of either disordered BCC or ordered B2 that solidifies directly from the liquid. In $\text{Hf}_{33}\text{Mo}_{34}\text{Ru}_{33}$ and $\text{Hf}_{25}\text{Mo}_{25}\text{Nb}_{25}\text{Ru}_{25}$, the B2 phase solidifies first, forming B2 dendrites; a disordered BCC phase then solidifies concurrently with more B2, forming two-phase inter-dendritic regions that are consistent with eutectic reactions. In $\text{Hf}_{25}\text{Mo}_{25}\text{Ta}_{25}\text{Ru}_{25}$ and $\text{Hf}_{20}\text{Mo}_{20}\text{Nb}_{20}\text{Ta}_{20}\text{Ru}_{20}$, the disordered BCC phases solidify first, followed by solidification of the B2 phase in Hf/Ru-enriched regions. Additional phases form from the remaining segregated liquid later in the solidification process. These microstructural observations are generally consistent with the Scheil curves predicted *via* CALPHAD (CALculation of PHASE Diagrams) methods, shown in Figures 15(a) and (b). The exception is $\text{Hf}_{25}\text{Mo}_{25}\text{Ta}_{25}\text{Ru}_{25}$, which did not form a distinct combination of BCC and B2 phases in the as-cast condition. The Scheil curve for $\text{Hf}_{25}\text{Mo}_{25}\text{Ta}_{25}\text{Ru}_{25}$ first predicts the formation of a disordered BCC phase, followed by a B2 phase.

The following solidification pathways were determined from the microstructural observations:

Similar to the other W-containing alloys, $\text{Hf}_{25}\text{Nb}_{25}\text{Ru}_{25}\text{W}_{25}$ first forms W-enriched BCC dendrites with the segregation of Hf, Nb, and Ru to the inter-dendritic regions. Within these inter-dendritic regions, large continuous islands of B2 have formed, along with B2 grains that outline the dendritic arms and others that are elongated in the direction of the grain

boundaries. The size and shape of these B2 grains, coupled with the low content of Ru (<10 at. pct) in both the inter- and intra-dendritic regions, indicate that they formed directly from the liquid. Further cooling after solidification may have resulted in the B2 nanoparticles observed in the dendritic regions. Solid-state precipitation of the nano-scale B2 is discussed in more depth in Section IV-A-1.

In $\text{Hf}_{33}\text{Mo}_{34}\text{Ru}_{33}$, the B2 phase first forms large dendrites; the remaining liquid potentially reaches a eutectic composition and forms an alternating lamellar microstructure of micron-scale B2 and BCC grains. The proposed solidification pathway is $L \rightarrow L + \text{HfRu} \rightarrow \text{HfRu} + \text{BCC} (\text{Mo})$. While any binary reactions and compositions are necessarily modified by the presence of the third element, the Hf-Ru binary contains a steep eutectic and a Ru concentration of 33 at. pct would fall on the pro-eutectic B2 side of the diagram, consistent with the observed morphologies. The two-phase region of the $\text{Hf}_{33}\text{Mo}_{34}\text{Ru}_{33}$ Scheil curve has the shallowest slope of all the alloys (Figure 15), which is consistent with the narrow-freezing ranges of eutectic materials; it is predicted that 58 pct of the solid forms between 2211.0 °C and 2209.5 °C.

In $\text{Hf}_{25}\text{Mo}_{25}\text{Nb}_{25}\text{Ru}_{25}$ (Figure 4(a) and (c)), the size of the large HfRu–B2 microstructural regions and the elongation of the smaller B2 particles perpendicular to the large structures indicate the large B2 regions solidified first. The small B2 particles then began to precipitate from the liquid and grew in the direction of the solidification front. Some regions (Figure 4(b) and (d)) lack the large B2 structures, but elongation of the B2 “feathers” towards observable grain boundaries indicates similar precipitation and growth along a solidification front. Continuous rejection of Mo and Nb from the B2 phase into the liquid would result in the formation of the nano-scale BCC regions visible in between the B2 particles, followed by the solidification of the last (Mo,Nb)-enriched liquid at the grain boundaries. Similar to $\text{Hf}_{33}\text{Mo}_{34}\text{Ru}_{33}$, the predicted Scheil curve for $\text{Hf}_{25}\text{Mo}_{25}\text{Nb}_{25}\text{Ru}_{25}$ is quite shallow in the two-phase regime, suggesting a eutectic reaction.

The disordered BCC dendrites in $\text{Hf}_{20}\text{Mo}_{20}\text{Nb}_{20}\text{Ta}_{20}\text{Ru}_{20}$ are enriched in Mo and Ta, indicating that they solidified first and were depleted in the remaining liquid. The (Hf,Ru)-B2 would have nucleated on the surface of the BCC dendrites, resulting in the observed rings; the formation of the B2 phase would also reject Mo, Nb, and Ta back into the liquid, resulting in the higher concentration of these elements in Phase 3 which solidified from the last liquid.

Of the Hf-containing alloys, only $\text{Hf}_{25}\text{Mo}_{25}\text{Ta}_{25}\text{Ru}_{25}$ does not form a combination of BCC and B2 phases in the as-cast condition. In the first phase to form, Phase 1, some segregation of Mo and Ta to the intra-dendritic regions and Hf and Ru to the inter-dendritic regions is measurable but the magnitude of the segregation is the smallest of among all the alloys and there are no distinct phase boundaries except for the transition to the intergranular phases. Therefore, $\text{Hf}_{25}\text{Mo}_{25}\text{Ta}_{25}\text{Ru}_{25}$ likely formed as a single-phase alloy, and the rejection of Hf results in the formation of the intergranular

Table V. Identified Phases and Calculated Lattice Parameters of the Heat-Treated Alloys

Alloy	Condition	Phase	Prototype	Lattice Parameter (Å)
Hf ₃₃ Mo ₃₄ Ru ₃₃	40 h at 1500 °C	B2	CsCl	3.230
	40 h at 1500 °C	BCC	W	3.145
Hf ₂₅ Mo ₂₅ Nb ₂₅ Ru ₂₅	40 h at 1600 °C	B2	CsCl	3.225
	40 h at 1600 °C	B2/BCC	—	3.224
Hf ₂₅ Mo ₂₅ Ta ₂₅ Ru ₂₅	40 h at 1600 °C	B2	CsCl	3.227
Hf ₂₀ Mo ₂₀ Nb ₂₀ Ta ₂₀ Ru ₂₀	40 h at 1600 °C	B2	CsCl	3.229
	40 h at 1600 °C	B2/BCC	—	3.240
Hf ₂₅ Nb ₂₅ Ru ₂₅ W ₂₅	40 h at 1600 °C	B2	CsCl	3.224
	40 h at 1600 °C	BCC	W	3.200

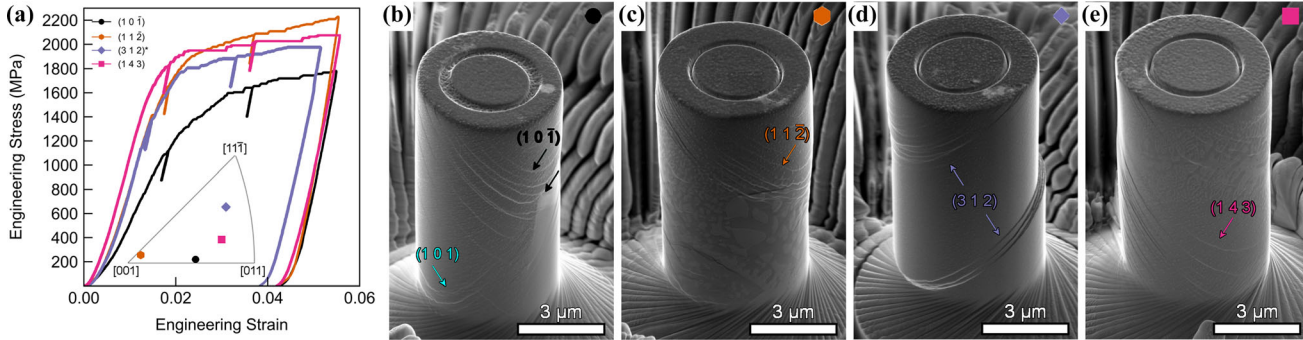


Fig. 13—(a) Micropillar compression stress–strain curves for all four micropillars investigated. Curves are colored and labeled according to the maximum resolved shear-stress (MRSS) plane. The (312) pillar was selected for subsequent (S)TEM analysis (marked by an asterisk). The inset shows the compression axis direction for each pillar, colored, and marked accordingly. (b) through (e). Surface morphology of deformed micropillars. The MRSS planes are annotated according to the coloring in (a). Additional slip traces in (b). (MRSS plane (101)) along the (101) plane are noted in cyan. Variations in the B2 precipitate morphology are evident in (c) and (e), where large grains of the B2 phase significantly impact the slip morphology (Color figure online).

phases from the remaining liquid. As noted previously, this result is inconsistent with the predicted Scheil curve (Figure 15(a)), which predicts the formation of both BCC and B2 phases during solidification. Under the current non-equilibrium solidification conditions, it is possible that the formation of a distinct B2 phase was suppressed by the speed of solidification. After heat treatment at 1600 °C, Phase 1 does decompose into two phases. One has a composition much closer to the other observed B2 phases (47.0 at. pct Hf, 39.2 at. pct Ru) and the other has a high concentration of BCC elements (34.9 at. pct Mo, 28.7 at. pct Ta).

After heat treatment, the coarsening of pre-existing phases and nucleation of new HfRu–B2 particles indicates the B2 phase is stable to at least 1600 °C (or 1500 °C in the case of Hf₃₃Mo₃₄Ru₃₃).

1. Nanoparticle regions in the Hf-containing alloys

Designing two-phase BCC + B2 alloys with precipitates stable at potential use temperatures of 1300 °C to 1400 °C is desirable for advanced high temperature applications. The nanoparticle regions observed in Hf₃₃Mo₃₄Ru₃₃, Hf₂₅Mo₂₅Nb₂₅Ru₂₅, Hf₂₀Mo₂₀Nb₂₀Ta₂₀Ru₂₀, and Hf₂₅Nb₂₅Ru₂₅W₂₅ present a starting point for alloy design utilizing HfRu–B2 precipitates to strengthen a BCC matrix. The size of the nanoparticles, particularly in contrast with the coarse B2 grains that

clearly derived from the liquid, suggest they formed after solidification was complete and during cooling of the solid-disordered BCC phases. This indicates that they might be subject to a solution and aging behavior pathway as commonly utilized for processing Ni-based superalloys. In the Hf–Ru binary-phase diagram, there exists a steep solvus line dividing the BCC–Hf field from the BCC–Hf + B2–HfRu phase field from 8 to 11 at. pct Ru in Hf. A binary BCC Hf–Ru alloy along this line would have solutionizable B2 precipitates of varying volume fractions. The compositions of the as-cast nanoparticle regions range from 3 to 12 at. pct Ru, which lie near that solvus line. Similarly, after heat treatment at 1600 °C, the formerly single-phase BCC regions (≈ 10 at. pct Ru) in HT-Hf₂₀Mo₂₀Nb₂₀Ta₂₀Ru₂₀ formed a significant volume fraction of new B2 nanoparticles.

CALPHAD predictions were made on all of the compositions of the nanoparticle regions observed in the as-cast and heat-treated alloys. An example set of phase and temperature predictions is presented in Figure 15(c) for the precipitated dendrite cores in HT-Hf₂₀Mo₂₀Nb₂₀Ta₂₀Ru₂₀ (Hf_{11.1}Mo_{27.6}Nb_{22.3}Ta_{29.8}Ru_{9.3}). Experimentally this region did not form nanoparticles upon cooling but formed them upon aging at 1600 °C for 40 hours and would be a likely candidate for a composition with solutionable particles. Only two

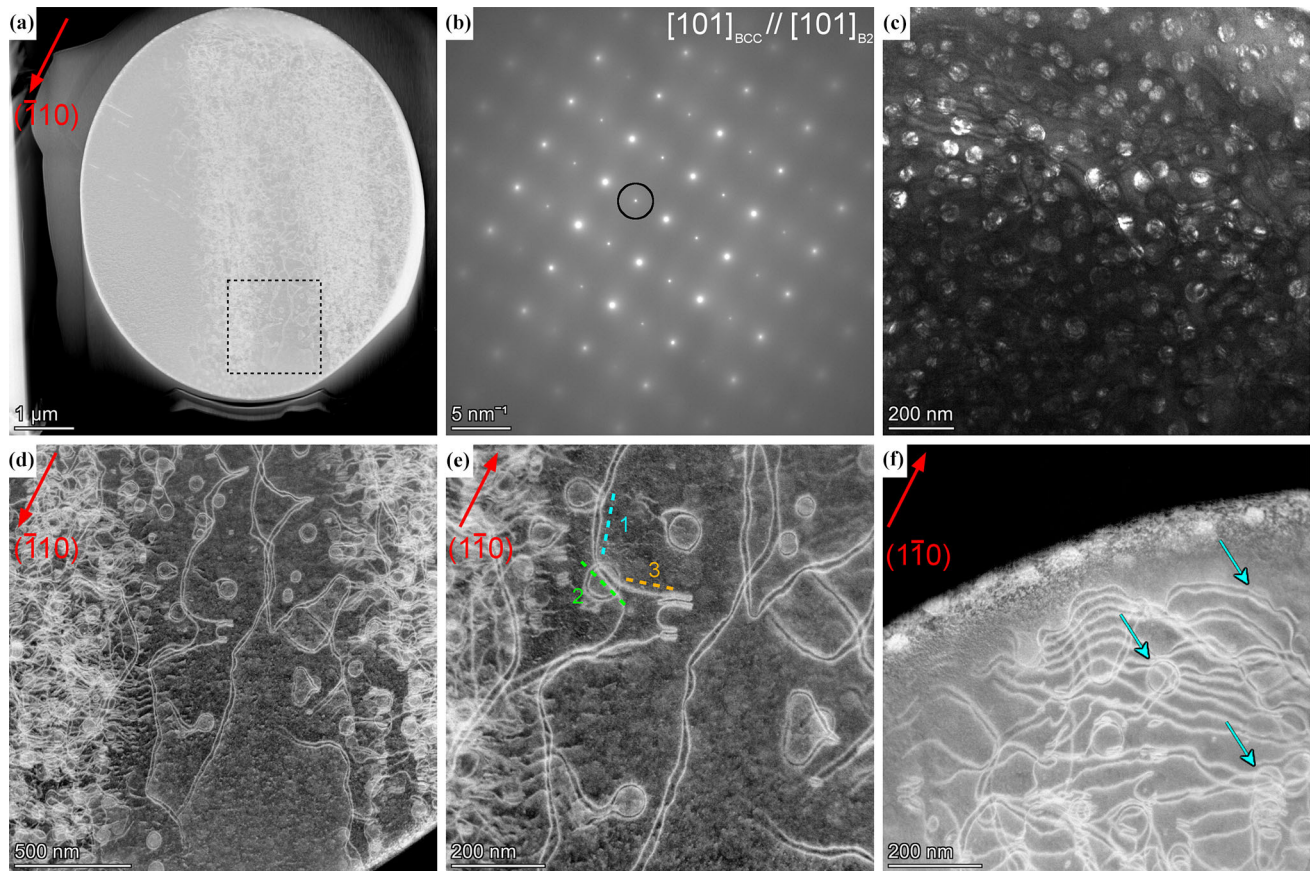


Fig. 14—(a) STEM overview of sample prepared from the (312) pillar in Figures 13(a) and (d). Sample was prepared so the foil normal is near the (312) plane. Dashed lines in (a) correspond to the region where dislocation trace analysis was performed in (d), (e). (b) SAED pattern acquired from the [101] zone axis. The black circle indicates the placement of the objective aperture for subsequent dark-field (DF) imaging of the B2 precipitates. (c) DF TEM image of the B2 nanoparticle precipitates near the top of the sample. Black wavy lines present in this image are dislocations interacting with precipitates. (d) through (f) ADF STEM images of dislocation structure in the deformed micropillar. Two-beam conditions are noted in red. Dislocations between the two nanoparticle and dislocation dense regions were selected for detailed analysis. These dislocations are paired, indicating cooperative shearing of the B2 precipitates. Dislocations are also looped around dislocations, indicating both Orowan bowing and precipitate-shearing mechanisms are active. Trace analysis was performed on segments 1 to 3 in (e), of the same dislocation. The line directions for these segments are $[-1.7, 2.3, 1.6]$, $[1.83, 0.23, -2.65]$, and $[1, 1.85, -2.45]$ for segments 1, 2, and 3, respectively. (f) Dislocation morphology near the top of the pillar. Regions with B2 particles undergoing shearing are noted with arrows.

phases are predicted by Thermo-Calc to be in equilibrium from 500 K to 3000 K: a disordered BCC phase and an ordered B2 phase with a volume fraction of approximately 0.22 (close to the experimentally measured B2 volume fraction of 0.29). The volume fractions are nearly constant with temperature. This is representative of the predictions for the rest of the nanoparticle regions, with only changes to the volume fraction of the B2 phase and the appearance of a minor amount of disordered HCP phase at low temperature varying from alloy to alloy. Interestingly, the B2 phase always persists to melting unless the Ru content is reduced to 1 to 2 at. pct (with Nb substitution). Further investigation of these compositions will be necessary to determine if the formation of nanoparticles is a result of the non-equilibrium solidification conditions or if Thermo-Calc is overpredicting the stability of the HfRu–B2 precipitates.

A similar approach could be taken with other Ru-containing RMPEAs that form B2 nanoparticles. $\text{Ti}_{20}\text{Al}_{20}\text{V}_{20}\text{Ru}_{20}$ contained a large number of small TiRu–B2 precipitates after annealing at 1200 °C for 24

hours.^[61] Similarly, the formation of HfCo–B2 nanoscale precipitates in disordered (Nb,Mo)–BCC regions was reported by Panina *et al.* in as-cast and annealed Hf–Co–Mo–Nb alloys.^[62,63] It is likely BCC + B2 alloys derived from those two-phase regions would also be capable of a solution and aging-processing pathway.

2. Composition of the HfRu–B2 phase

Of the investigated alloying elements, the formation of HfRu appears significantly more thermodynamically stable than any other B2 phase. While the single-phase B2 $\text{Mo}_{25}\text{Nb}_{25}\text{Ta}_{25}\text{Ru}_{25}$ alloy demonstrates that Mo, Nb, and Ta can all participate and form a B2 intermetallic at sufficiently high concentrations of Ru, the HfRu–B2 phase is always formed when Hf is present. These observations are consistent with the known enthalpies of formation reported for HfRu (-91.8 kJ/mol^[64]), NbRu (-9 kJ/mol^[65]), and the lack of B2 phases in the Mo- and W-Ru binaries. While the formation enthalpy of TaRu has not been reported to the authors' knowledge, it is likely similar in magnitude to the formation

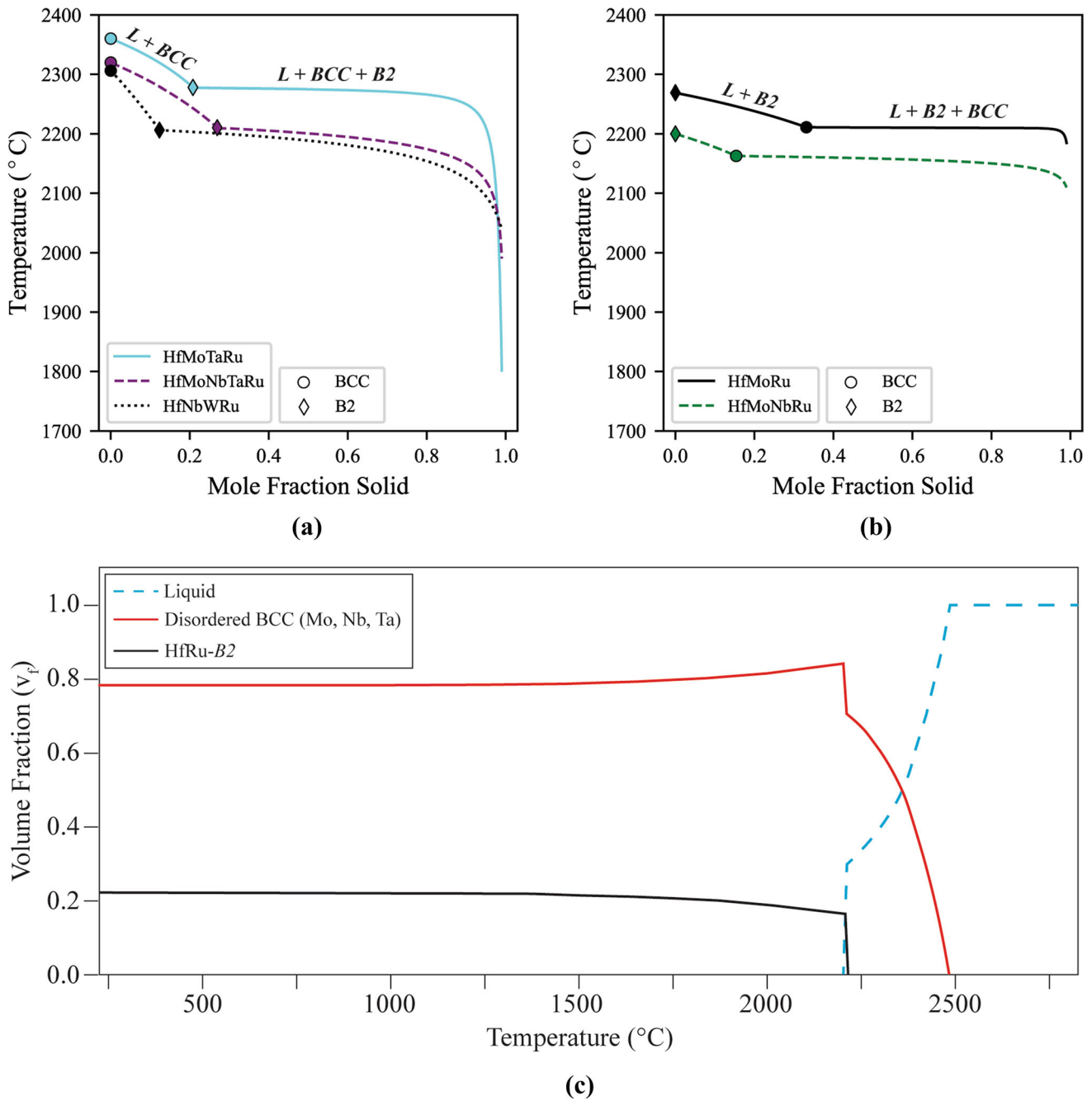


Fig. 15—(a) Predicted Scheil curves for alloys where the first phase to solidify is disordered BCC. (b) Predicted Scheil curves for alloys where the first phase to solidify is HfRu–B2. Predictions were made in Thermo-Calc using the TCHEA4 database.^[60] Alloy legend is arranged in order of liquidus temperature, and the phase (B2 or BCC) markers indicate where the respective phase begins to solidify from the liquid. (c) Phase volume fraction versus temperature for Hf_{11.1}Mo_{27.6}Nb_{22.3}Ta_{29.7}Ru_{9.3}. Two phases, a B2 phase and a disordered BCC phase, are predicted to be stable until melting.

enthalpy of NbRu due to the chemical similarity of Nb and Ta and the similarity of formation enthalpies for the Group IV elements (HfRu (– 91.8 kJ/mol), TiRu (– 77.0 kJ/mol^[64]), and ZrRu (– 68.7 kJ/mol^[64]).

As measured by SEM-EDS and EPMA, the HfRu–B2 phase can accommodate up to 17 at. pct total of the other elements (Mo, Nb, Ta, W) after heat treatment at 1500/1600 °C, though there is a range of 3 to 17 at. pct (Tables III, IV and VI). After heat treatment, when Nb

and/or Ta were present in an alloy, the HfRu–B2 phase contained on average 6.7 at. pct Nb + Ta and 4.7 at. pct of Mo + W. In contrast, when Ti and Zr (with formation enthalpies greater than Nb or Ta but less than Hf) are present in combination with Hf, their solubility in the HfRu–B2 phase is significant at 11 to 15 at. pct.^[44,61] Considering a binary HfRu alloy within the BCC–Hf + HfRu–B2 phase field, the alloy would have an equilibrium B2 composition of 48 at. pct Hf and 52

at. pct Ru. The average composition of the investigated B2 phases was reduced to 47 at. pct Hf and 43.5 at. pct Ru, indicating that Ru is preferentially substituted for Mo, Nb, Ta, and W at 1500 °C/1600 °C in these compositions. In contrast, Hf was preferentially substituted for Zr in $\text{Hf}_{20}\text{Nb}_{20}\text{Ta}_{20}\text{Ru}_{20}\text{Zr}_{20}$ ^[44] and for Ti/Zr in $\text{Hf}_{20}\text{Ru}_{20}\text{Ti}_{20}\text{Zr}_{20}$.^[61] Overall, the composition of the HfRu–B2 phases in these multi-component systems appears to scale with formation enthalpy of the binary B2 phases.

B. Interaction of Dislocations with HfRu–B2 Precipitates

The interaction of dislocations with precipitates directly influences the extent of precipitate strengthening and resulting bulk mechanical properties. While the alloys in this investigation do not have carefully controlled microstructures in the bulk and small-scale testing may not be completely reflective of bulk properties, the more uniform and fine-scale BCC + B2 nanoparticle regions offer an opportunity study to dislocation-precipitate interactions *via* micromechanical testing. Micropillar compression experiments were performed in the two-phase BCC + B2 regions of the HT- $\text{Hf}_{20}\text{Mo}_{20}\text{Nb}_{20}\text{Ta}_{20}\text{Ru}_{20}$ alloy, and post-mortem (S)TEM analysis reveals complex dislocation behavior (Figures 13 and 14). Similar to other RMPEAs, the room-temperature deformation in the BCC phase of $\text{Hf}_{20}\text{Mo}_{20}\text{Nb}_{20}\text{Ta}_{20}\text{Ru}_{20}$ is accommodated largely by the motion of tortuous, wavy screw dislocations (Figures 14(d) and (e)).^[48,66–68] The long, paired segments in Figures 14(a), (d) through (f) are approximately screw in character. The surface slip traces and dislocation trace analysis (line direction determination) indicate that these predominantly screw-character dislocations can glide along higher-order planes, such as the (312) plane in Figure 13. Near the top and bottom surfaces of the sample, we observe some edge dislocations, indicating that their motion is sluggish compared to simple or pure BCC metals,^[66,69,70] but that edge segments are still more mobile than screws in this system at room temperature.

The dislocations present in Figures 14(d) through (f) are paired with a spacing ranging from 6 to 20 nm. Paired (or coupled) dislocations are frequently observed during shearing of ordered precipitates, as the successive motion of two dislocations through the ordered precipitate effectively preserves its original ordering.^[71] This coupled dislocation motion has been observed in many ordered B2 systems, including β brass,^[72,73] FeCo,^[74] NiAl,^[75] duplex steels,^[76] and other high-entropy alloys.^[77] The strong coupling between the dislocations in this system suggests that the energetic penalty for disordering the B2 phase, *i.e.*, the anti-phase boundary (APB) energy, is high. An estimate of the APB energy can be made by assuming that the shear stress necessary to shear the precipitates, τ_c , is equivalent to the Orowan bowing stress, τ_b . Dislocations would shear precipitates when the stress necessary to do so falls below the Orowan bowing stress, as is the case for small shearable particles;^[14] therefore, this assumption would yield an

estimate for the maximum APB energy. The Orowan bowing stress is equivalent to

$$\tau_b = \frac{Gb}{L}, \quad [2]$$

where G is the shear modulus of the matrix, b is the Burgers vector of the matrix, and L is the distance between the particles. The cutting stress is expected to be on the order of:

$$\tau_c \approx \frac{\gamma_{\text{APB}}}{b}, \quad [3]$$

where γ_{APB} is the APB energy.^[14]

A value of 69.8 GPa was calculated for G from a weighted average of the elemental shear moduli and the composition of the BCC phase reported in Table VI (see Supplemental Table 2 for exact values). The magnitude of the Burgers vector, $b = a/2(111)$, was calculated from the lattice parameter of the BCC phase determined by TEM in Section III–C and is equal to 0.283 nm. The average precipitate spacing, L , can be estimated by measuring the distance between the points in Figure 14(d) where the paired dislocations “pinch” together and equal to 104 nm. Using Eq. [2], τ_b is calculated to be 190 MPa; assuming τ_b is equivalent to τ_c , an APB energy of 54 mJ/m² is estimated, similar to other intermetallics.^[73] Alloying strategies that increase the APB energy would be desirable for further increasing strength.

Interestingly, Figure 14(e) displays the formation of several jogs near the segment selected for trace analysis. These jogged segments appear in pairs (*i.e.*, there are two jogs nearby), even though they are formed by a single dislocation (*i.e.*, the trailing dislocation in Figure 14(e)). They do not appear to be formed as a result of precipitate shearing by two paired dislocations that each form a single jog. There are also many paired dipole loops in the sample (Figure 14(e)) which form as a single-jogged screw dislocation with two nearby jogs advances and pinches off. The presence of many of these paired dipole loops suggests that this process is common during room-temperature deformation.

While this paired or coupled dislocation motion is a strong indication that precipitate shearing is a predominant deformation mechanism, there are also numerous instances of Orowan looping, where the dislocations bow out and pinch off around the precipitates rather than shear them. Many of these loops are visible in Figures 14(d) and (e) where the circular precipitates are outlined by the contrast from the looped dislocations. The presence of both shearing and looping may arise due to the polydispersity of nanoparticle sizes, where smaller precipitates are sheared, and larger precipitates exhibit bowing. However, the precipitate size distribution appears fairly narrow in this sample (Figure 13(c)), and there are several precipitates undergoing shearing (Figure 14(f)) that are larger than small precipitates that have been looped around by dislocations (Figures 14(e) and (f)). Thus, it is unlikely that the particle size is solely responsible for this behavior. The high stresses present during micropillar compression experiments may

Table VI. Identified Phases, Assigned Crystal Structures, and Their Compositions (At. Pct) as Measured by EDS of the Heat-Treated Alloys

Alloy	Region	Crystal Structure	Hf	Mo	Nb	Ru	Ta	W
Hf ₃₃ Mo ₃₄ Ru ₃₃ 40 h at 1500	Phase 1	B2	51.0	3.2	—	45.8	—	—
	Phase 2	BCC	3.0	90.0	—	7.0	—	—
	lamellar	B2 + BCC	22.6	53.6	—	23.8	—	—
	nanoparticle	B2 + BCC	5.1	85.3	—	9.7	—	—
Hf ₂₅ Mo ₂₅ Nb ₂₅ Ru ₂₅ 40 h at 1600	Phase 1	B2	44.9	5.5	6.8	42.7	—	—
	Phase 2	BCC	11.2	38.3	47.0	3.6	—	—
	nanoparticle	B2 + BCC	13.8	34.8	41.8	9.6	—	—
	Phase 1	B2	47.0	8.3	—	39.2	5.6	—
Hf ₂₅ Mo ₂₅ Ta ₂₅ Ru ₂₅ 40 h at 1600	Phase 2	—	27.3	34.9	—	8.4	28.7	—
	Phase 3	—	94.8	0.9	—	0.5	3.7	—
	Phase 4	—	62.7	15.3	—	6.6	15.4	—
	Phase 1	BCC	7.7	28.1	29.8	3.7	30.7	—
Hf ₂₀ Mo ₇₀ Nb ₂₀ Ta ₂₀ Ru ₂₀ 40 h at 1600	Phase 2	B2	47.2	2.8	2.5	44.1	3.5	—
	Phase 3	—	82.7	6.4	6.7	0.0	5.2	—
	nanoparticle	B2 + BCC (fine)	11.1	27.6	22.3	9.3	29.8	—
	nanoparticle	B2 + BCC (coarse)	16.2	20.9	27.3	12.5	23.1	—
Hf ₂₅ Nb ₂₅ Ru ₂₅ W ₂₅ 40 h at 1600	Phase 1, intra-dendritic region	BCC	2.6 to 18.1	—	32.0 to 69.1	0.0 to 7.9	—	14.5 to 65.3
	Phase 2	B2	46.5	—	5.8	45.6	—	2.1
	“fuzzy” W-rich region	—	4.8	—	20.2	1.6	—	73.4
	lamellar	B2 + BCC	5.2	—	19.8	2.5	—	72.6
nanoparticle	B2 + BCC (new)	10.2	—	34.2	5.8	—	—	49.8
	B2 + BCC (coarse)	15.8	—	42.3	11.2	—	—	30.8

Error is on the order of a few at. pct percent

Table VII. Compression Axis and Resulting Mechanical Properties of each Hf₂₀Mo₂₀Nb₂₀Ta₂₀Ru₂₀ Micropillar

Compression Axis $[h, k, l]$	Slip System with Highest Schmid Factor $(u,v,w)[h, k, l]$	Schmid Factor (m)	Yield Strength at 0.2 pct Offset (MPa)	Resolved Shear Stress on MRSS Plane (MPa)	Young's Modulus, E (GPa)
[0,4,9]	(1,0, $\bar{1}$)[1,1,1]	0.492	1250	616	173
[1,1,12]	(1,1, $\bar{2}$)[1,1,1]	0.497	1630	810	207
[3,5,7]	(3,1,2)[$\bar{1}$,1,1]	0.469	1769	830	188
[4,1,6]	(1,4,3)[$\bar{1}$, 1, 1]	0.500	1835	917	166

Table VIII. G-dot-b Analysis of Dislocations Observed in Hf₂₀Mo₂₀Nb₂₀Ta₂₀Ru₂₀ After Micropillar Compression

Burgers Vectors	(10 $\bar{1}$)			(0 $\bar{1}1$)		(1 $\bar{1}0$)		(1 $\bar{2}3$)	
	g	g.b	Visible? (Y/N)	g.b	Visible? (Y/N)	g.b	Visible? (Y/N)	g.b	Visible? (Y/N)
[111]	0	0	Y	0	N	0	Y	2	N
[$\bar{1}\bar{1}\bar{1}$]	2	-2	Y	-2	N	0	Y	-4	N
[$\bar{1}\bar{1}1$]	0	2	Y	2	N	2	Y	6	N
[$\bar{1}\bar{1}1$]	-2	0	Y	0	N	-2	Y	0	N

facilitate bowing in the case of a single dislocation arriving at the precipitate, though many of the looped precipitates appear to be looped by two dislocations. Stresses can also be elevated by multiple dislocations of the same Burgers vector piling up behind precipitates; many parallel dislocations are apparent in Figure 14(f). There may be additional complexity causing this dual behavior, such as interfacial structure and interactions between the lattice and misfit dislocations at the BCC–B2 interface,^[78] the slip transfer behavior from a higher-order (312) slip plane in the BCC phase to a (101) or (211) plane in the B2 phase, or other chemical effects at the BCC–B2 interface that hinder precipitate shearing. The details of the deformation mechanisms and the value of APB energies, interfacial structure, and the transition from shearing to looping, are actively being investigated. Nevertheless, the present results emphasize that the development of appropriate processing and aging workflows for controlling nanoparticle sizes and distributions, akin to that in Ni-based superalloys, will be effective in promoting high temperature strength in BCC–B2 alloys.

C. Implications for Design of Ru-Containing BCC + B2 Alloys

A coherent B2 precipitate in a BCC matrix would hypothetically provide high temperature strength and creep resistance if the precipitate is morphologically and thermodynamically stable at target temperatures. Ru appears to be a promising alloying addition for achieving stable coherent precipitates above 1200 °C in RMPEAs.

Overall, Ru consistently forms a B2 phase in the presence of Hf, forms only small volume fractions of other, less desirable phases, and the nanoparticle regions

previously described in Section IV–A–1 are suggestive of compositions that would have precipitates that can be solutioned and aged. The hardness values reported by Detor *et al.* for the investigated alloys range from 623 to 859 HV,^[45] on par with the hardest materials reported in the literature, demonstrating a potential for high strengths in these alloys.^[44,79] The compositions of the two-phase nanoparticle regions contain much less Ru and Hf than the equiatomic compositions, with a range of Ru content of 1.6 to 12.8 at. pct and 4.8 to 18.8 at. pct of Hf. These values are consistent with the BCC/BCC + B2 solvus lines in the HfRu phase diagram^[80] and are beneficial for reducing weight and cost of future alloys. Ti and Zr both participate significantly in the HfRu–B2 phase when present with Hf, providing an alternative route for increased light weighting if Ti or Zr could be substituted for Hf.^[44,61] Further property adjustments of the B2 phases may be possible by modifying the composition of the other minor elements that partition to that phase. The B2 phases are also stable above 1500 °C, significantly above new target temperatures of 1300 °C to 1400 °C for turbine applications. However, significant challenges and questions remain for developing these alloys.

One challenge to developing coherent Ru-based B2 phases is the small lattice parameters of the known B2 phases in comparison to the lattice parameters of desirable matrix elements like Nb or Ta, which possess significant room-temperature ductility and high melting temperatures. The lattice parameter of Nb is 3.301 Å, and the lattice parameters of HfRu and ZrRu are 3.225 Å (– 2.3 pct misfit) and = 3.253 Å (– 1.5 pct), respectively. Additions of small atoms like Al,^[81,82] Cr ($a_{Cr} = 2.878$ Å^[83]), Mo ($a_{Mo} = 3.147$ Å^[84]), V ($a_V = 3.026$ Å,^[85]) and W ($a_W = 3.1648$ Å^[83]) can reduce the matrix lattice parameter of Nb, as shown by the less

than 1 pct misfit between the as-cast HfRu nanoparticles and the surrounding (Mo, Nb, Ta)-rich matrix in $\text{Hf}_{20}\text{Mo}_{20}\text{Nb}_{20}\text{Ta}_{20}\text{Ru}_{20}$ (Figure 9). These additions would need to be carefully balanced with their impacts on room-temperature tensile ductility; only V does not have a detrimental impact on ductility,^[86,87] but it possess a relatively low melting point and a low melting oxide that can cause failure due to penetration along grain boundaries at high temperatures.^[1]

Another challenge for these alloys is the development of a processing pathway to produce an evenly dispersed high volume fraction of B2 particles in a BCC matrix. The two-phase nanoparticle regions measured present a starting point for alloys that might possess a solution and aging window comparable to Ni- and Co-based superalloys. However, the two-phase γ - γ' phase field in the Ni-Al binary is much narrower than the BCC + B2 phase field in the HfRu binary, indicating high enough volume fractions of solutionable B2 precipitates may be more difficult to achieve due to the steepness of the solvus line. However, given the complex compositions proposed, more understanding is needed of the ternary and quaternary spaces involved. Alternative, less explored, processing methods are possible if the solvus temperature of the B2 phases cannot be suppressed to accommodate a true solution and aging protocol. Powder-based methods that suppress the formation of the B2 phase through rapid cooling could be used to produce a bulk piece, followed by an aging protocol to evolve the B2 precipitates.

V. CONCLUSION

The microstructures of a series of as-cast and annealed Ru-containing RMPEAs have been characterized in detail. The investigated RMPEAs form high volume fractions of intermetallic phases and undergo complex dendritic, eutectic, and peritectic solidification reactions. The major findings of this investigation are

- In the presence of Hf, the RMPEAs preferentially form a HfRu-B2 phase, with the remaining elements forming a disordered BCC phase. The HfRu-B2 phase formed both during solidification, in the form of B2 dendrites and other large B2 grains, and during further cooling in the solid, in the form of HfRu-B2 nanoparticles that precipitated in the disordered BCC phases.
- In as-cast $\text{Hf}_{20}\text{Mo}_{20}\text{Nb}_{20}\text{Ta}_{20}\text{Ru}_{20}$, the lattice mismatch between the nanoparticles and the (Mo, Nb, Ta)-disordered BCC lattice was determined by TEM to be < 1 pct.
- After 40 hours anneals at 1500 °C to 1600 °C, all previously observed phases coarsened and new HfRu-B2 nanoparticles precipitated in $\text{Hf}_{20}\text{Mo}_{20}\text{Nb}_{20}\text{Ta}_{20}\text{Ru}_{20}$ and $\text{Hf}_{25}\text{Nb}_{25}\text{Ru}_{25}\text{W}_{25}$.
- Micropillar compression cylinders were milled into the BCC + nanoparticle B2 regions of $\text{Hf}_{20}\text{Mo}_{20}\text{Nb}_{20}\text{Ta}_{20}\text{Ru}_{20}$ and compressed to a strain of approximately 5 pct. Post-mortem TEM analysis

found both shearing of precipitates by dislocations and bowing of dislocations around nanoparticles.

In conclusion, Ru additions present an opportunity to develop RMPEAs with BCC + B2 microstructures that are coherent and stable above 1200 °C. Further investigation is necessary to determine if the HfRu-based B2 phases can be solutionable, coherent, and present in high enough volume fractions to beneficially impact high temperature mechanical properties.

ACKNOWLEDGMENTS

The authors gratefully acknowledge the support of ONR Grant N00014-181-2392. This research was performed while GHB held an NRC Research Associateship award at the Air Force Research Laboratory. KM was supported by a National Science Foundation Graduate Research Fellowship under Grant No. 2139319. SEM, XRD, and WDXRF were conducted in the MRL Shared Experimental Facilities, supported by the NSF MRSEC Program under Award #DMR2308708. The authors also thank Ashlea Patterson for her assistance analyzing the XRD data.

CONFLICT OF INTEREST

The authors declare that they have no conflict of interest.

SUPPLEMENTARY INFORMATION

The online version contains supplementary material available at <https://doi.org/10.1007/s11661-024-07368-x>.

REFERENCES

1. D. O. Hobson: Tech. rep., Atomic Energy Commission, 1962.
2. R.T. Begley, D.L. Harrod, and R.E. Gold: Tech. Rep., Westinghouse Astronuclear Laboratory, Pittsburgh, 1968. <https://doi.org/10.1007/978-1-4684-9120-3>.
3. in *Refractory Alloy Technology for Space Nuclear Power Applications*, R.H.J. Cooper, and E.E. Hoffman, eds., United States Department of Energy, 1984, p. 279.
4. J.W. Yeh, Y.L. Chen, S.J. Lin, and S.K. Chen: *Mater. Sci. Forum*, 2007, vol. 560, pp. 1–9. <https://doi.org/10.4028/www.scientific.net/msf.560.1>.
5. S.P. Wang, E. Ma, and J. Xu: *Intermetallics*, 2019, vol. 107, pp. 15–23. <https://doi.org/10.1016/j.intermet.2019.01.004>.
6. C. Zhang, B.E. MacDonald, F. Guo, H. Wang, C. Zhu, X. Liu, Y. Kang, X. Xie, Y. Zhou, K.S. Vecchio, and E.J. Lavernia: *Scripta Mater.*, 2020, vol. 188, pp. 16–20. <https://doi.org/10.1016/j.scriptamat.2020.07.006>.

7. Y.C. Huang, Y.C. Lai, Y.H. Lin, and S.K. Wu: *J. Alloys Compd.*, 2021, vol. 855, p. 157404. <https://doi.org/10.1016/j.jallcom.2020.157404>.
8. L. Wang, S. Chen, B. Li, T. Cao, B. Wang, L. Wang, Y. Ren, J. Liang, and Y. Xue: *Mater. Sci. Eng. A*, 2021, vol. 814, p. 141234. <https://doi.org/10.1016/j.msea.2021.141234>.
9. E.J. Rapperport and A.L. Geary: Tech. Rep., Nuclear Metals, Inc., West Concord, 1963.
10. O.N. Senkov, S.I. Rao, T.M. Butler, and K.J. Chaput: *J. Alloys Compd.*, 2019, vol. 808, p. 151685. <https://doi.org/10.1016/j.jallcom.2019.151685>.
11. S. Dasari, A. Sharma, V. Soni, Z. Kloenne, H. Fraser, and R. Banerjee: *Microsc. Microanal.*, 2022, <https://doi.org/10.1017/s1431927622012053>.
12. D.M. Jin, Z.H. Wang, J.F. Li, B. Niu, and Q. Wang: *Rare Met.*, 2022, vol. 41(8), pp. 2886–93. <https://doi.org/10.1007/s12598-022-01971-w>.
13. N. Yurchenko, E. Panina, S. Zherebtsov, and N. Stepanov: *Materialia*, 2021, vol. 16, p. 101057. <https://doi.org/10.1016/j.mtla.2021.101057>.
14. R.C. Reed: *The Superalloys*, 1st ed. Cambridge University Press, New York, 2006.
15. C. Gadelmeier, Y. Yang, U. Glatzel, and E.P. George: *Cell Rep. Phys. Sci.*, 2022, vol. 3(8), p. 100991. <https://doi.org/10.1016/j.xcrp.2022.100991>.
16. Q. Wang, Z. Li, S. Pang, X. Li, C. Dong, and P.K. Liaw: *Entropy*, 2018, <https://doi.org/10.3390/e20110878>.
17. O.N. Senkov, C. Woodward, and D.B. Miracle: *Jom*, 2014, vol. 66(10), pp. 2030–42. <https://doi.org/10.1007/s11837-014-1066-0>.
18. D. Schliephake, A.E. Medvedev, M.K. Imran, S. Obert, D. Fabijanic, M. Heilmaier, A. Molotnikov, and X. Wu: *Scripta Mater.*, 2019, vol. 173, pp. 16–20. <https://doi.org/10.1016/j.scriptamat.2019.07.033>.
19. D.B. Miracle, M.H. Tsai, O.N. Senkov, V. Soni, and R. Banerjee: *Scripta Mater.*, 2020, vol. 187, pp. 445–52. <https://doi.org/10.1016/j.scriptamat.2020.06.048>.
20. S. Laube, S. Schellert, A.S. Tirunilai, D. Schliephake, B. Gorr, H.-J. Christ, A. Kauffmann, and M. Heilmaier: *Acta Mater.*, 2021, <https://doi.org/10.1016/j.actamat.2021.117217>.
21. V. Soni, B. Gwalani, T. Alam, S. Dasari, Y. Zheng, O.N. Senkov, D. Miracle, and R. Banerjee: *Acta Mater.*, 2020, vol. 185, pp. 89–97. <https://doi.org/10.1016/j.actamat.2019.12.004>.
22. T.E. Whitfield, E.J. Pickering, C.E. Talbot, C.N. Jones, H.J. Stone, and N.G. Jones: *Scripta Mater.*, 2020, vol. 180, pp. 71–76. <https://doi.org/10.1016/j.scriptamat.2020.01.028>.
23. Y.G. Dong, S. Chen, N.N. Jia, Q.H. Zhang, L. Wang, Y.E. Xue, and K. Jin: *Tungsten*, 2021, vol. 3(4), pp. 406–14. <https://doi.org/10.1007/s42864-021-00111-8>.
24. T.E. Whitfield, G.J. Wise, H.J. Stone, and N.G. Jones: *Appl. Phys. Lett.*, 2021, <https://doi.org/10.1063/5.0068045>.
25. K. Kadirvel, Z. Kloenne, J.K. Jensen, H. Fraser, and Y. Wang: *Appl. Phys. Lett.*, 2021, <https://doi.org/10.1063/5.0065522>.
26. P. Kumar, S.J. Kim, Q. Yu, J. Ell, M. Zhang, Y. Yang, J.Y. Kim, H.K. Park, A.M. Minor, E.S. Park, and R.O. Ritchie: *Acta Mater.*, 2023, vol. 245, p. 118620. <https://doi.org/10.1016/j.actamat.2022.118620>.
27. N. Yurchenko, E. Panina, A. Tojibaev, S. Zherebtsov, and N. Stepanov: *Mater. Res. Lett.*, 2022, vol. 10(12), pp. 813–23. <https://doi.org/10.1080/21663831.2022.2109442>.
28. S. Laube, A. Kauffmann, S. Schellert, S. Seils, S. Tirunilai, C. Greiner, Y.M. Eggeler, B. Gorr, H. Christ, and M. Heilmaier: *Sci. Technol. Adv. Mater.*, 2022, <https://doi.org/10.1080/14686996.2022.2132118>.
29. B. Zhao, G. Chen, S. Lv, X. Fu, and W. Zhou: *J. Alloys Compd.*, 2022, vol. 896, p. 163129. <https://doi.org/10.1016/j.jallcom.2021.163129>.
30. X.P. Zhu, N. Gao, Z.C. Bai, K. Wang, J.Q. Yao, Z.T. Fan, Z.D. Wang, and X.W. Liu: *Mater. Lett.*, 2022, vol. 325, p. 132897. <https://doi.org/10.1016/j.matlet.2022.132897>.
31. T.E. Whitfield, N.L. Church, H.J. Stone, and N.G. Jones: *J. Alloys Compd.*, 2021, <https://doi.org/10.1016/j.jallcom.2022.168369>.
32. A.J. Knowles, D. Dye, R.J. Dodds, A. Watson, C.D. Hardie, and S.A. Humphry-Baker: *Appl. Mater. Today*, 2021, vol. 23, p. 101014. <https://doi.org/10.1016/j.apmt.2021.101014>.
33. N. Yurchenko, E. Panina, D. Shaysultanov, S. Zherebtsov, and N. Stepanov: *Materialia*, 2021, vol. 20, p. 101225. <https://doi.org/10.1016/j.mtla.2021.101225>.
34. N. Yurchenko, E. Panina, L. Rogal, L. Shekhawat, S. Zherebtsov, and N. Stepanov: *Mater. Res. Lett.*, 2022, vol. 10(2), pp. 78–87. <https://doi.org/10.1080/21663831.2021.2022033>.
35. G. Ghosh and G.B. Olson: *Acta Mater.*, 2007, vol. 55(10), pp. 3281–3303. <https://doi.org/10.1016/j.actamat.2007.01.036>.
36. A. Misra, G. Ghosh, and G.B. Olson: *J. Phase Equilib. Diffus.*, 2004, vol. 25(6), pp. 507–14. <https://doi.org/10.1361/15477020421025>.
37. H. Okamoto: *J. Phase Equilib.*, 1991, vol. 12(3), pp. 395–97. <https://doi.org/10.1007/BF02649940>.
38. G.F. Hurley and J.H. Brophy: *J. Less-Common Met.*, 1964, vol. 7, pp. 267–77. [https://doi.org/10.1016/0022-5088\(64\)90023-2](https://doi.org/10.1016/0022-5088(64)90023-2).
39. N. David, T. Benlaharche, J.M. Fiorani, and M. Vilasi: *Intermetallics*, 2007, vol. 15(12), pp. 1632–37. <https://doi.org/10.1016/j.intermet.2007.07.013>.
40. R.M. Waterstrat and R.C. Manuszewski: *J. Less-Common Met.*, 1976, vol. 48, pp. 151–58.
41. A. Grytsiv, P. Rogl, H. Schmidt, and G. Giester: *J. Phase Equilib.*, 2003, vol. 24(6), pp. 511–27. <https://doi.org/10.1361/105497103772084552>.
42. J.L. Murray: *Bull. Alloys Phase Diagr.*, 1982, vol. 3(2), pp. 216–21. <https://doi.org/10.1007/BF02892392>.
43. L. Perring, F. Bussy, J.C. Gachon, and P. Feschotte: *J. Alloys Compd.*, 1999, vol. 284(1–2), pp. 198–205. [https://doi.org/10.1016/S0925-8388\(98\)00911-6](https://doi.org/10.1016/S0925-8388(98)00911-6).
44. C. Frey, R. Silverstein, and T.M. Pollock: *Acta Mater.*, 2022, vol. 229, p. 117767. <https://doi.org/10.1016/j.actamat.2022.117767>.
45. A. Detor, S. Oppenheimer, R. Casey, and C. Crawford: *Data Brief*, 2022, <https://doi.org/10.1016/j.dib.2022.108582>.
46. *E562-19e I. Standard Test Method for Determining Volume Fraction by Systematic Manual Point Count*, ASTM International, West Conshohocken, PA, 2020. <https://doi.org/10.1520/E0562-19E01>.
47. M.D. Uchic and D.M. Dimiduk: *Mater. Sci. Eng. A*, 2005, vol. 400–401, pp. 268–78. <https://doi.org/10.1016/j.msea.2005.03.082>.
48. G.H. Balbus, S.I. Rao, O.N. Senkov, and E.J. Payton: *Acta Mater.*, 2024, vol. 262, p. 119401. <https://doi.org/10.1016/j.actamat.2023.119401>.
49. D. Norfleet, D. Dimiduk, S. Polasik, M. Uchic, and M. Mills: *Acta Mater.*, 2008, vol. 56(13), pp. 2988–3001. <https://doi.org/10.1016/j.actamat.2008.02.046>.
50. F. Mompou and R. Xie: *J. Microsc.*, 2021, vol. 282(1), p. 84.
51. H. Okamoto, M. E. Schlesinger and E. M. Mueller: in *Alloy Phase Diagrams*, vol. 3, chap. Mo (Molybdenum) Binary Alloy Phase Diagrams, 2016, pp. 489–98. <https://doi.org/10.31399/asm.hb.v03.a0006178>.
52. R. Zhao, J. Wang, H. Yuan, B. Hu, Y. Du, and Z. Tan: CALPHAD: Comput. Coupling Phase Diagr. Thermochem., 2020, vol. 69, p. 101766. <https://doi.org/10.1016/j.calphad.2020.101766>.
53. H. Okamoto: *J. Phase Equilib.*, 1991, vol. 12(2), pp. 211–14.
54. A. Kaufmann, E. J. Rapperport, M. F. Smith, J. Wulff, J. Brophy, N. J. Grant, B. C. Giessen, A. Taylor, and N. Doyle: Tech. Rep., United States Air Force, 1960.
55. T.A. Parthasarathy, S.I. Rao, D.M. Dimiduk, M.D. Uchic, and D.R. Trinkle: *Scripta Mater.*, 2007, vol. 56(4), pp. 313–16. <https://doi.org/10.1016/j.scriptamat.2006.09.016>.
56. G. Laplanche, P. Gadaud, L. Perriere, I. Guillot, and J.P. Couzinie: *J. Alloys Compd.*, 2019, vol. 799, pp. 538–45. <https://doi.org/10.1016/j.jallcom.2019.05.322>.
57. F.H. Featherston and J.R. Neighbours: *Phys. Rev.*, 1963, vol. 130, pp. 1324–33. <https://doi.org/10.1103/PhysRev.130.1324>.
58. C.N. Reid, J.L. Routbort, and R.A. Maynard: *J. Appl. Phys.*, 1973, vol. 44(3), pp. 1398–99. <https://doi.org/10.1063/1.1662365>.
59. B.H. Chen and H.F. Franzen: *J. Less-Common Met.*, 1989, vol. 153(2), pp. 13–19. [https://doi.org/10.1016/0022-5088\(89\)90133-1](https://doi.org/10.1016/0022-5088(89)90133-1).
60. TCHEA4, ThermoCalc Software, 2022.
61. Y. Yamabe-Mitarai, K. Yanao, Y. Toda, I. Ohnuma, and T. Matsunaga: *J. Alloys Compd.*, 2022, vol. 911, p. 164849. <https://doi.org/10.1016/j.jallcom.2022.164849>.
62. E. Panina, N. Yurchenko, A. Tojibaev, M. Mishunin, S. Zherebtsov, and N. Stepanov: *J. Alloys Compd.*, 2022, vol. 927, p. 167013. <https://doi.org/10.1016/j.jallcom.2022.167013>.

63. E. Panina, N. Yurchenko, G. Salishchev, S. Zhrebtsov, and N. Stepanov: *Int. J. Refract. Met. Hard Mater.*, 2023, vol. 115, p. 106297. <https://doi.org/10.1016/j.ijrmhm.2023.106297>.
64. Q. Guo and O.J. Kleppa: *J. Alloys Compd.*, 2001, vol. 321(2), pp. 169–82. [https://doi.org/10.1016/S0925-8388\(01\)00956-2](https://doi.org/10.1016/S0925-8388(01)00956-2).
65. M.Y. Benarchid, N. David, J.M. Fiorani, M. Vilasi, and T. Benlaharche: *Thermochim. Acta*, 2009, vol. 482(1–2), pp. 39–41. <http://doi.org/10.1016/j.tca.2008.10.010>.
66. F. Wang, G.H. Balbus, S. Xu, Y. Su, J. Shin, P.F. Rottmann, K.E. Knipling, J.C. Stinville, L.H. Mills, O.N. Senkov, I.J. Beyerlein, T.M. Pollock, and D.S. Gianola: *Science*, 2020, vol. 370(6512), pp. 95–101. <https://doi.org/10.1126/science.aba3722>.
67. R.R. Eleti, N. Stepanov, and S. Zhrebtsov: *Scripta Mater.*, 2020, vol. 188, pp. 118–23. <https://doi.org/10.1016/j.scriptamat.2020.07.028>.
68. R.R. Eleti, N. Stepanov, N. Yurchenko, D. Klimenko, and S. Zhrebtsov: *Scripta Mater.*, 2021, vol. 200, p. 113927. <https://doi.org/10.1016/j.scriptamat.2021.113927>.
69. S. Rao, B. Akdim, E. Antillon, C. Woodward, T. Parthasarathy, and O. Senkov: *Acta Mater.*, 2019, vol. 168, pp. 222–36. <https://doi.org/10.1016/j.actamat.2019.02.013>.
70. S. Rao, C. Woodward, B. Akdim, O. Senkov, and D. Miracle: *Acta Mater.*, 2021, vol. 209, p. 116758. <https://doi.org/10.1016/j.actamat.2021.116758>.
71. R.W. Kozar, A. Suzuki, W.W. Milligan, J.J. Schirra, M.F. Savage, and T.M. Pollock: *Metall. Mater. Trans. A*, 2009, vol. 40A(7), pp. 1588–1603. <https://doi.org/10.1007/s11661-009-9858-5>.
72. D.G. Morris and M.A. Morris: *J. Mater. Sci.*, 1991, vol. 26(7), pp. 1734–40. <https://doi.org/10.1007/BF00543595>.
73. M.H. Yoo, T. Takasugi, S. Hanada, and O. Izumi: *Mater. Trans. JIM*, 1990, vol. 31(6), pp. 435–42. <https://doi.org/10.2320/matertrans1989.31.435>.
74. I. Baker: *Mater. Sci. Eng. A*, 1995, vol. 192–193, pp. 1–13. [http://doi.org/10.1016/0921-5093\(94\)03200-9](http://doi.org/10.1016/0921-5093(94)03200-9).
75. R. Taillard and A. Pineau: *Mater. Sci. Eng.*, 1982, vol. 56(3), pp. 219–31. [https://doi.org/10.1016/0025-5416\(82\)90097-0](https://doi.org/10.1016/0025-5416(82)90097-0).
76. M.C. Ha, J.-M. Koo, J.-K. Lee, S.W. Hwang, and K.-T. Park: *Mater. Sci. Eng. A*, 2013, vol. 586, pp. 276–83. <https://doi.org/10.1016/j.msea.2013.07.094>.
77. J.-P. Couzinie, M. Heczko, V. Mazanova, O.N. Senkov, M. Ghazisaeidi, R. Banerjee, and M.J. Mills: *Acta Mater.*, 2022, vol. 233, p. 117995. <https://doi.org/10.1016/j.actamat.2022.117995>.
78. Z.T. Kloenne, J.-P. Couzinie, M. Heczko, R. Groger, G.B. Viswanathan, W.A. Clark, and H.L. Fraser: *Scripta Mater.*, 2023, vol. 223, p. 115071. <https://doi.org/10.1016/j.scriptamat.2022.115071>.
79. C.K. Borg, C. Frey, J. Moh, T.M. Pollock, S. Gorsse, D.B. Miracle, O.N. Senkov, B. Meredig, and J.E. Saal: *Sci. Data*, 2020, vol. 7(1), pp. 1–6. <https://doi.org/10.1038/s41597-020-00768-9>.
80. V.N. Eremenko, L.S. Kriklya, V.G. Khoruzhaya, and T.D. Shtepa: *Poroshkovaya Metallurgiya*, 1992, vol. 19(5), pp. 463–66.
81. S. Ge, H. Fu, L. Zhang, H. Mao, H. Li, A. Wang, W. Li, and H. Zhang: *Mater. Sci. Eng. A*, 2020, vol. 784, p. 139275. <https://doi.org/10.1016/j.msea.2020.139275>.
82. Z.Q. Xu, Z.L. Ma, M. Wang, Y.W. Chen, Y.D. Tan, and X.W. Cheng: *Mater. Sci. Eng. A*, 2019, vol. 755, pp. 318–22. <https://doi.org/10.1016/j.msea.2019.03.054>.
83. S. Naidu, A. Sriramamurthy, and P. Rao: *Bull. Alloys Phase Diagr.*, 1984, vol. 5(3), pp. 289–92.
84. J.L. Murray: *Bull. Alloys Phase Diagr.*, 1981, vol. 2(2), pp. 185–92.
85. J.F. Smith, D.M. Bailey, and O.N. Carlson: *Bull. Alloys Phase Diagr.*, 1982, vol. 2(4), pp. 469–73. <https://doi.org/10.1007/BF02876166>.
86. R. Huang, J. Tan, W. Li, Q. Dong, C.J. Li, X.M. Qin, S.F. Guo, and Y.P. Lu: *Intermetallics*, 2022, <https://doi.org/10.1016/j.intermet.2022.107472>.
87. M. Wang, Z.L. Ma, Z.Q. Xu, and X.W. Cheng: *Mater. Sci. Eng. A*, 2021, <https://doi.org/10.1016/j.msea.2021.140848>.

Publisher's Note Springer Nature remains neutral with regard to jurisdictional claims in published maps and institutional affiliations.

Springer Nature or its licensor (e.g. a society or other partner) holds exclusive rights to this article under a publishing agreement with the author(s) or other rightsholder(s); author self-archiving of the accepted manuscript version of this article is solely governed by the terms of such publishing agreement and applicable law.